nature communications

Article

https://doi.org/10.1038/s41467-026-69335-x

Reverse hydrogen spillover accelerates electrocatalytic nitrate reduction to ammonia on Ru/WO_{3-x} in acidic media

Received: 18 January 2025

Accepted: 29 January 2026

Published online: 16 February 2026

Check for updates

Weijie Zhu[1,2,3,8], Yu-Chang Lin[4,8], Jianlong Cong[5,8], Mengting Zhao[2,8], Jiahao Li[2], Cong Hao[2], Jun Jia[2], Xinlu Wang[6], Yunhui Huang[5], Yan-Gu Lin[4,7] ✉, Gang Yang[1] ✉, Fen Yao[3] ✉ & Hanfeng Liang[2] ✉

The electrocatalytic nitrate reduction reaction (NO_3^-RR) offers a promising route to sustainable ammonia synthesis, potentially replacing the energy-intensive Haber-Bosch process. While often studied in neutral or alkaline media, NO_3^-RR in acidic conditions is particularly relevant due to widespread industrial acidic nitrate wastewater, yet it remains challenging due to corrosion and dominant hydrogen evolution. To address this, we designed a corrosion-resistant Ru/WO_{3-x} heterostructure that spatially separates proton and nitrate adsorption sites. Here, we show that a reverse hydrogen spillover effect, where the WO_{3-x} support stores and transports protons to surface Ru active sites, dramatically enhances hydrogenation kinetics and suppresses parasitic hydrogen evolution. This catalyst achieves an ammonia Faradaic efficiency of 94.09% at a high current density of 500 mA cm^{-2} and a working potential of 0.026 V vs. reversible hydrogen electrode. Furthermore, we demonstrate a sulfide-nitrate "batterolyzer" with a discharge power density of 43.4 mW cm^{-2}. This work reveals an effective proton-management strategy for efficient acidic NO_3^-RR, advancing its potential for coupled ammonia synthesis and wastewater treatment.

Ammonia is a crucial feedstock widely used in many chemical production processes. It also serves as an excellent hydrogen storage medium. The current industrial ammonia production is dominated by the Haber-Bosch process, which involves massive energy consumption and CO_2 emissions[1]. Therefore, developing green and sustainable ammonia synthesis technology is of great importance. In this context, electrocatalytic nitrate reduction reaction (NO_3^-RR), which converts nitrate effluents into ammonia, has emerged as a promising alternative. Unlike the Haber-Bosch process that requires a direct supply of H_2 at high temperatures and pressures, NO_3^-RR can mildly hydrogenate nitrates to ammonia using protons from aqueous effluents under ambient conditions[2]. However, NO_3^-RR is currently mostly explored in neutral and alkaline media, which necessitates additional water molecule dissociation to produce hydrogen species, often

[1]Electrocatalysis and New Energy Materials Research Center, School of Materials Engineering, Suzhou University of Technology, Suzhou 215500, China. [2]State Key Laboratory of Physical Chemistry of Solid Surfaces, Tan Kah Kee Innovation Laboratory, College of Chemistry and Chemical Engineering, Xiamen University, Xiamen 361005, China. [3]Key Laboratory of Preparation and Applications of Environmentally Friendly Material of the Ministry of Education, College of Chemistry, Jilin Normal University, Changchun 130103, China. [4]National Synchrotron Radiation Research Center, Hsinchu 300092, Taiwan. [5]State Key Laboratory of Materials Processing and Die & Mould Technology, School of Materials Science and Engineering, Huazhong University of Science and Technology, Wuhan 430074, China. [6]School of Chemistry and Environmental Engineering, Changchun University of Science and Technology, Changchun 130022, China. [7]Department of Materials Science and Engineering, National Yang Ming Chiao Tung University, Hsinchu 300093, Taiwan. [8]These authors contributed equally: Weijie Zhu, Yu-Chang Lin, Jianlong Cong, Mengting Zhao. ✉e-mail: lin.yg@nsrrc.org.tw; gyang@szut.edu.cn; yaof@jlnu.edu.cn; hfliang@xmu.edu.cn

resulting in high overpotentials. Moreover, the volatilization of ammonia in alkaline conditions complicates ammonia capture, potentially leading to losses and environmental issues[3]. In contrast, NO_3^-RR in acidic conditions directly forms valuable ammonium salts (e.g., NH_4NO_3), effectively preventing ammonia volatilization. Additionally, the hydrogenation kinetics are facilitated in proton-rich environments. Given that acidic nitrate effluents are widely distributed in mining, metallurgical, and petrochemical industries, acidic NO_3^-RR is of practical importance for both environmental protection and ammonium production.

The primary challenge of acidic NO_3^-RR lies in the highly corrosive environment, which severely limits the selection of suitable electrocatalysts. Most high-performance neutral and alkaline NO_3^-RR electrocatalysts, such as Fe, Co, and Cu-based oxides[4,5], cannot withstand these harsh acidic conditions. Even acid-stable phosphides or nitrides often undergo surface reconstructions during the NO_3^-RR, forming hydroxides that quickly dissolve in acidic environments[6]. This essentially leaves only acid-resistant noble metals like Rh, Ir, and Ru as viable options. While these noble metals exhibit high corrosion resistance and catalytic activity, they also possess a favorable hydrogen adsorption ability[7]. This can not only facilitate NO_3^-RR hydrogenation steps but also promote the dihydrogen coupling for H_2 release (Fig. 1a), especially in acidic media, where the kinetics of competing hydrogen evolution reaction (HER) are accelerated. Moreover, strongly adsorbed protons may weaken the adsorption and activation of nitrates on these metal sites[8], consequently reducing the ammonia Faradaic efficiency. As a result, current acidic NO_3^-RR catalysts have so far failed to achieve practical ammonia production with high activity and Faradaic efficiency at high cathodic current densities, i.e., higher than 200 mA cm^{-2}.

Using Ru, a relatively affordable platinum group catalyst with high NO_3^-RR activity, as a demonstration, we address this key challenge by geometrically separating proton and nitrate adsorption sites through introducing WO_3 as support for Ru nanoparticles. WO_3 is a typical proton storage and spillover material ($WO_3 + xH + xe^- \rightarrow H_xWO_3$)[9,10], and was chosen over alternatives (e.g., MoO_3[11], TiO_2[12], and Al_2O_3[13]) due to its excellent corrosion resistance as well as high proton insertion potential and storage capacity in acidic media[14]. In addition, WO_3 exhibits intrinsically poor HER activity[15], meaning the inserted protons are less likely to combine and form H_2. Instead, the inserted protons in WO_3 support are expected to migrate to NO_3^-RR hydrogenation sites connected to the surface-exposed Ru atoms through electric driving force (Fig. 1b). Our proposed design showcases a reverse hydrogen spillover behavior at the Ru/WO_3 heterostructure. While reverse hydrogen spillover has been observed in several metal-oxide combinations (e.g., Ir/HfO_2[16], Ru/WO_{3-x}[17], $La_2Sr_2PtO_{7+\delta}$[18]) with enhanced HER kinetics, its effect in acidic NO_3^-RR, which involves significantly more complicated reaction pathways and more proton/electron transfer, has not yet been explored.

In this work, we systematically investigated the reverse hydrogen spillover phenomenon at the Ru/WO_{3-x} heterostructure (x represents oxygen vacancies), and further demonstrated its crucial role in promoting the NO_3^-RR hydrogenation kinetics through combined experimental and theoretical analyses. The catalyst achieved record-high NO_3^-RR performance in acidic media, with a practical current density of 500 mA cm^{-2} at a positive potential of 0.026 V vs. reversible hydrogen electrode (RHE), along with a high ammonia Faradaic efficiency of 94.09%. We further assembled a sulfide-nitrate "batterolyzer" via coupling cathodic acidic NO_3^-RR and anodic alkaline sulfide oxidation reaction (S^{2-}OR) using Ru/WO_{3-x} and Co_9S_8 as catalysts, respectively. This device achieved a peak discharge power density of 43.4 mW cm^{-2} at 100 mA cm^{-2}, along with the production of ammonium and polysulfide, showcasing great potential in pollutant treatment and high-value chemical production.

Results

Synthesis and structural characterization of the Ru/WO_{3-x} catalyst

The Ru/WO_{3-x} catalyst was prepared by a three-step method (Fig. 2a). Specifically, the nanorod-like $(NH_4)_xWO_3$ precursor was first hydrothermally synthesized on a titanium felt substrate (Supplementary Fig. 1), which was then immersed in a $RuCl_3$ solution for cation adsorption, followed by calcination in a reductive atmosphere to form the Ru/WO_{3-x} catalyst. For comparison, WO_{3-x} and Ru individuals were also synthesized (see details in Methods). X-ray diffraction (XRD) pattern of the Ru/WO_{3-x} reveals the presence of both WO_3 (JCPDS No. 85-2460) and Ru (JCPDS No. 89-3942) with hexagonal close-packed (hcp) crystal structure (Fig. 2b). The broad diffraction peaks of Ru in the Ru/WO_{3-x} likely result from highly dispersed Ru nanoparticles loaded on the WO_{3-x} support. Interestingly, the diffraction intensity of WO_{3-x} (002) and (200) planes reversed after Ru loading. This suggests that the anchored Ru nanoparticles influence the preferential crystal orientation of the WO_{3-x} support along the c axis. A similar phenomenon was observed in previous studies on Ir-loaded W_5O_{14}[19]. Previous experiments confirmed that protons tend to insert into WO_3 (002) planes, forming strong hydrogen bonding with bridged oxygen atoms[20], which could enhance proton storage capacity and consequently promote the reverse hydrogen spillover possibility.

In addition to phase identification, scanning electron microscopy (SEM) images reveal abundant Ru/WO_{3-x} nanorods vertically grown on the surface of titanium fibers, forming a dense and intertwined waterweed-like morphology (Supplementary Fig. 2). Although the SEM images may not clearly distinguish the bi-phase structure, the high angle annular dark field scanning transmission electron microscopy (HAADF-STEM) image, along with the corresponding elemental linear and planar scans, indicate the presence of numerous Ru nanoparticles located on the surface of a WO_{3-x} nanorod (Fig. 2c). Further investigation using high resolution transmission electron microscopy

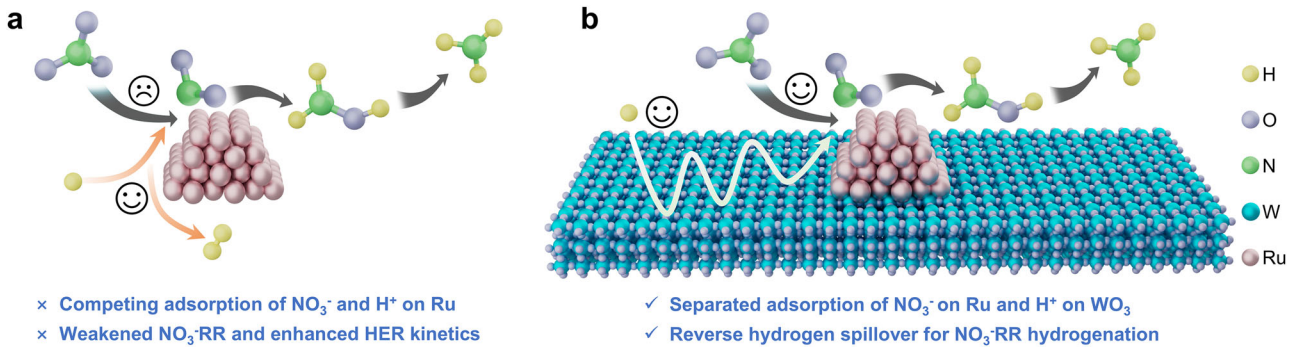

Fig. 1 | Schematic illustration of the adsorption pathways for protons and nitrates on different catalytic models, highlighting their advantages and disadvantages. **a** Ru metal and **b** Ru/WO_3 heterostructure.

https://doi.org/10.1038/s41467-026-69335-x

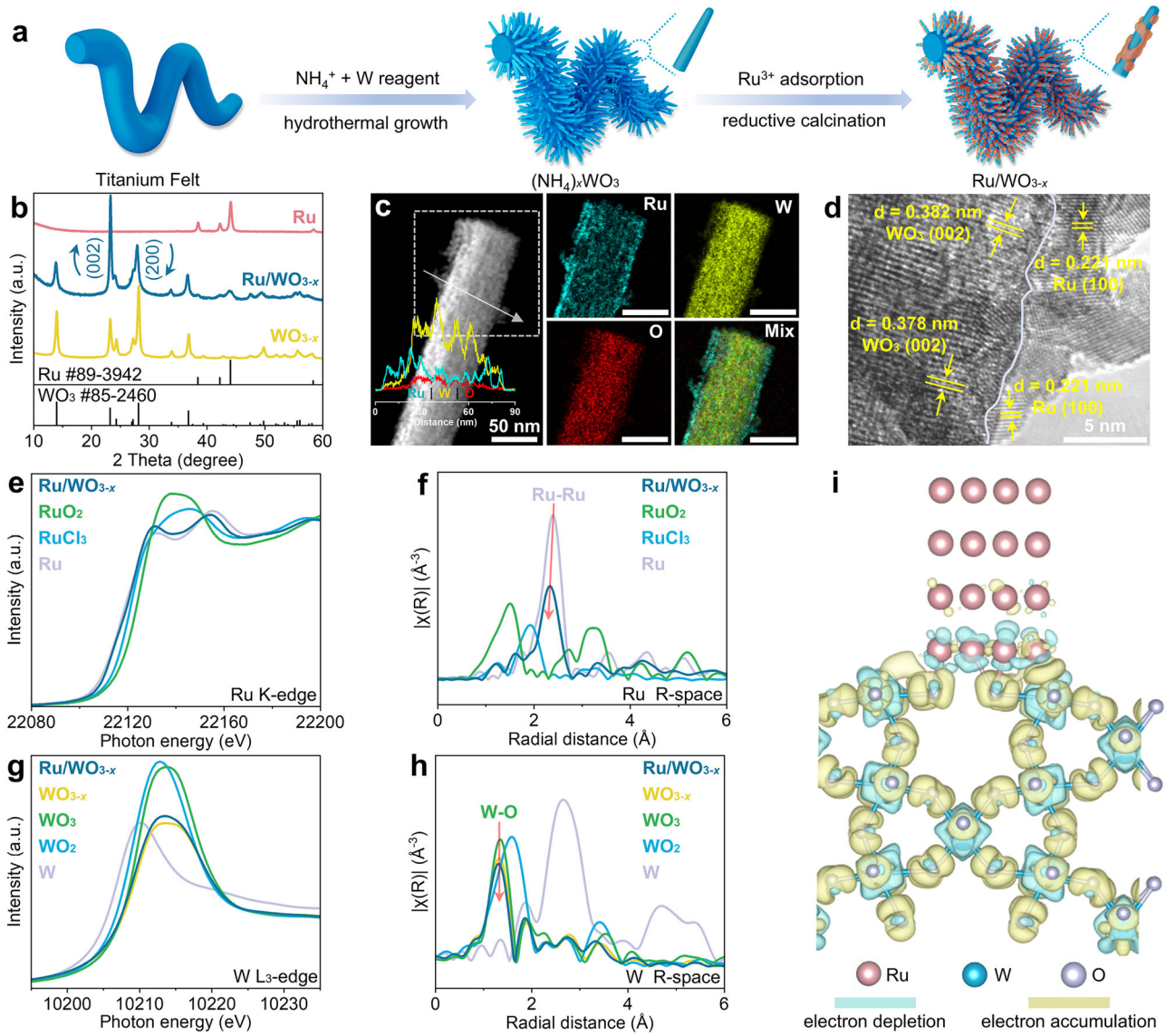

Fig. 2 | Phase composition and electronic structure identification of Ru/WO_{3-x}. **a** Schematic illustration of the synthesis process. **b** XRD patterns. **c** HAADF-STEM image with corresponding elemental linear and planar scans. **d** HRTEM image. **e** Ru K-edge XANES and (**f**) EXAFS spectra. **g** W L_3-edge XANES and (**h**) EXAFS spectra. **i** Differential charge density plot. Source data for Fig. 2 are provided as a Source Data file.

(HRTEM) reveals a distinct heterointerface between Ru (100) and WO_{3-x} (002) planes (Fig. 2d). Notably, the Ru (100) plane exhibits a slightly contracted lattice spacing of 0.221 nm compared to bulk Ru (0.235 nm, Supplementary Fig. 3), indicating lattice strain induced by the heterointerface formation. In contrast, the WO_{3-x} (002) plane maintains nearly identical spacings (0.382 and 0.378 nm) to pristine WO_{3-x} (0.38 nm, Supplementary Fig. 4). This lattice shrinkage of the former may be attributed to the strong metal-support interaction (SMSI) between the Ru nanoparticles and WO_{3-x} support. These characterizations collectively confirm that the Ru nanoparticles in the Ru/WO_{3-x} catalyst are uniformly distributed on the surface of the WO_{3-x} nanorod support, contributing to the formation of abundant heterointerfaces.

Identification the SMSI effect in the Ru/WO_{3-x} catalyst

The SMSI in the Ru/WO_{3-x} was further investigated by X-ray absorption spectroscopy (XAS). Ru K-edge X-ray absorption near edge structure (XANES) spectra reveal that the absorption edge of the Ru/WO_{3-x} lies between that of Ru and $RuCl_3$ controls (Fig. 2e). This observation suggests that the Ru metal sites in the Ru/WO_{3-x} are electron-deficient. By further plotting first derivative curves and calculating the standard oxidation state of Ru species against average photon energy at half-peak width, it is estimated that the Ru oxidation state in the Ru/WO_{3-x} is approximately +0.23 (Supplementary Fig. 5). Additionally, Fourier transformed Ru K-edge extended X-ray absorption fine structure (EXAFS) spectra demonstrate the presence of a distinct Ru-Ru metal bond with a bond length of 2.33 Å in the Ru/WO_{3-x}, which is slightly shorter than that in the Ru control (2.42 Å, without phase correction, Fig. 2f and Supplementary Fig. 6), well in line with the HRTEM result. This phenomenon is further confirmed by wavelet transform spectra (Supplementary Fig. 7). This indicates that the SMSI in the Ru/WO_{3-x} induces Ru lattice shrinkage, consistent with HRTEM observations. According to the absorption edge of W L_3-edge XANES spectra and the derived first derivative curves[21,22], the estimated W oxidation state follows the trend of W, WO_2, Ru/WO_{3-x}, WO_{3-x}, and WO_3 from smallest to largest (Fig. 2g and Supplementary Fig. 8). The W oxidation state in the Ru/WO_{3-x} is ca. +4.7, lower than that in the WO_{3-x} (+5.6). Combined with the Ru and W oxidation state analysis, it can be inferred that electrons transfer from Ru metal to W sites at the Ru/WO_{3-x} heterointerfaces, thus enhancing the SMSI effect. The W L_3-edge EXAFS spectra indicate that the first shell W-O coordination intensity shows a progressive weakening

https://doi.org/10.1038/s41467-026-69335-x

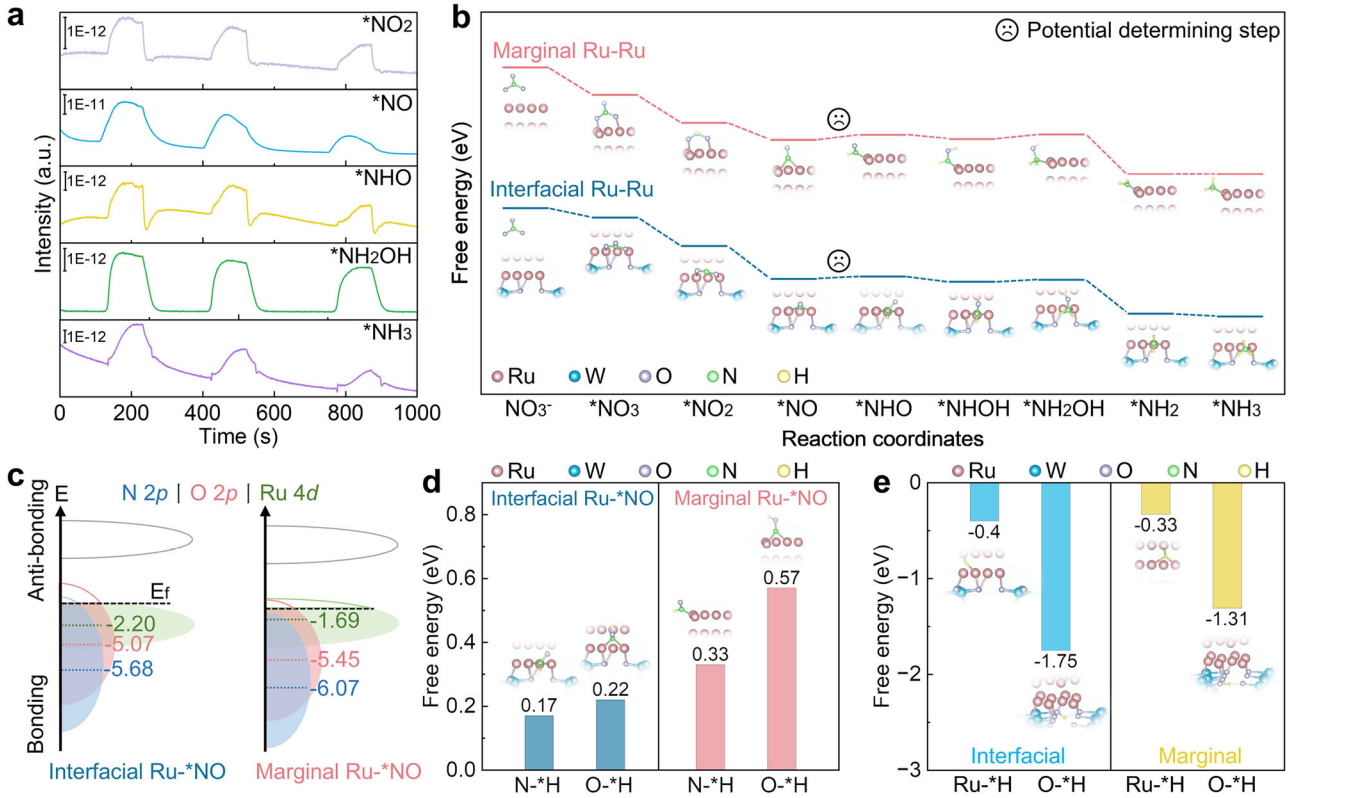

Fig. 3 | Identification of the active centers for NO_3^-RR on Ru/WO_{3-x}. **a** DEMS spectra. **b** Reaction pathway free energy diagrams for interfacial and marginal Ru-Ru dual-site adsorption models. **c** Schematic of the simulated band centers and (**d**) hydrogenation free energy on N or O site for interfacial and marginal Ru-*NO adsorption models. **e** Proton adsorption free energy diagrams for interfacial and marginal Ru and O sites in the initial Ru/WO_{3-x} model. Insets in (**b**), (**d**) and (**e**) show the corresponding atomic models. Source data for Fig. 3 are provided as a Source Data file.

from WO_3 control to WO_{3-x} to Ru/WO_{3-x} (Fig. 2h, Supplementary Fig. 9 and 10), suggesting substantial local structural disorder. This observation, combined with the continuous positive shift in O 1*s* binding energy observed by X-ray photoelectron spectroscopy (XPS, Supplementary Fig. 11), provides compelling evidence for the generation of oxygen vacancies during the reductive calcination process.[23] The above results indicate the presence of SMSI in the Ru/WO_{3-x}, characterized by significant charge rearrangement. This is further corroborated by Raman analysis, which reveals a noticeable red shift in both the W-O-W bending vibration (298 and 360 cm^{-1}) and the O-W-O stretching vibration (747 and 837 cm^{-1}) of the WO_{3-x} after Ru loading (Supplementary Fig. 12)[24]. In addition to the spectroscopic analysis, the optimized Ru/WO_{3-x} structure model simulated by density functional theory (DFT) reveals that the interfacial Ru atoms are bonded to adjacent W atoms via bridged O bonds (Supplementary Fig. 13 and Data 1), though the Ru-O bonds were not observed in the Ru K-edge EXAFS spectra due to the high-energy X-ray incident light. The differential charge density distribution further reveals that the interfacial Ru atoms are electron-deficient, while both the conjoined O and W atoms at the interface are comparatively electron-enriched (Fig. 2i), well aligning with the spectroscopic analysis.

Mechanistic Insights into Acidic NO_3^-RR over the Ru/WO_{3-x} catalyst

To investigate the impact of the SMSI in the Ru/WO_{3-x} on the acidic NO_3^-RR, we conducted DFT calculations to identify the potential actives sites in the Ru/WO_{3-x}. According to the online differential electrochemical mass spectrometry (DEMS) result of the Ru/WO_{3-x} in 1 M H_2SO_4/0.1 M KNO_3 mixed electrolytes at 0.2 V vs. RHE (without *iR* correction, see detailed configuration in Supplementary Fig. 14), the acidic NO_3^-RR pathway of the Ru/WO_{3-x} involves initial electro-adsorption of NO_3^- to form *NO_3, followed by continuous hydrogenation to *NO_2, *NO, *NHO, *NHOH, *NH_2OH, *NH_2, and *NH_3 in sequence (Fig. 3a)[25]. The *NH_3 finally undergoes a non-electrochemical desorption and spontaneous protonation to NH_4^+. The thermodynamic free energy of the electrochemical process was specifically compared using two dual-sites NO_3^- adsorption models (i.e., interfacial Ru-Ru sites with charge rearrangement and marginal Ru-Ru sites with regular charge distribution, Fig. 3b). The calculation results indicate that the electro-adsorption and initial hydrogenation steps towards *NO in both models are exothermic, suggesting the spontaneous reaction pathways (Supplementary Table 1). However, the subsequent two hydrogenation steps on metal-connected *N sites (i.e., the transformation of *NO to *NHO and *NHOH to *NH_2OH) are endothermic, with the former being the potential-determining step. The required Gibbs free energy of the interfacial Ru-Ru sites is 0.17 eV, much lower than marginal Ru-Ru sites (0.33 eV), suggesting that the interfacial electron-deficient Ru sites can reduce the thermodynamic energy barrier of hydrogenation steps and thus become the active centers of the Ru/WO_{3-x} for NO_3^-RR. The remaining steps, such as hydrogenation of *NHO, *NH_2OH, and *NH_2, are spontaneous for both models.

To further investigate the influence of electronic structure of active Ru sites on the hydrogenation step of the connected N site, we simulated the projected density of states (PDOS) (Supplementary Fig. 15) and calculated the corresponding band centers of the interfacial and marginal Ru-*NO adsorption models. The *p* band center of the N site adjacent to the interfacial Ru site is −5.68 eV, higher than that adjacent to the marginal Ru site (−6.07 eV, Fig. 3c). Consequently, the former thus requires a smaller hydrogenation free energy (0.17 eV) than the latter (0.33 eV) at the potential determining step (Fig. 3d). Similarly, the calculated *p* band center of the O site in the interfacial Ru*-NO model is −5.07 eV, also higher than that in the marginal Ru*-NO

https://doi.org/10.1038/s41467-026-69335-x

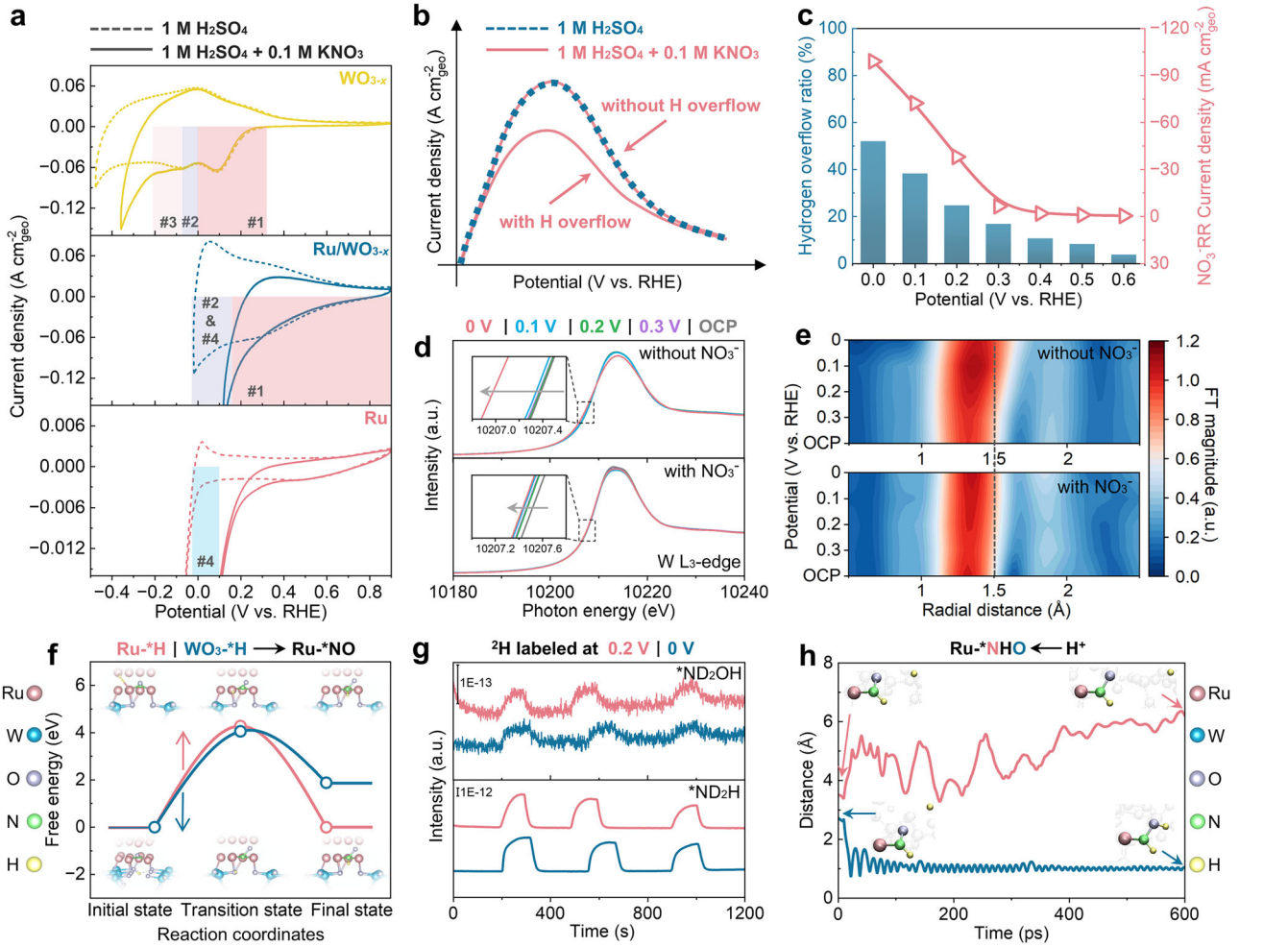

Fig. 4 | Identification of hydrogenation way for NO_3^-RR on Ru/WO_{3-x}. **a** CV curves with 80% *iR* correction. **b** Simulated LSV curves for proton desorption. **c** Calculated H spillover ratio and the corresponding NO_3^-RR polarization curve without *iR* correction. **d** In situ W L_3-edge XANES and (**e**) EXAFS spectra in 1 M H_2SO_4 with and without 0.1 M KNO_3 (The presented potentials are not *iR*-corrected). **f** Transition state comparison for simulated H transfer pathways from adjacent Ru-*H or interfacial WO_3-*H to interfacial Ru-*NO; insets show the initial, transition, and final state models. **g** ^2H isotope-labeled DEMS spectra. **h** AIMD simulated distance between the N or O site of the interfacial Ru-*NHO model and protons from the electrolyte; insets show the initial and final state models. Source data for Fig. 4 are provided as a Source Data file.

model (−5.45 eV, Fig. 3c). Correspondingly, the hydrogenation free energy at the interface-related O site (0.22 eV) is smaller than that at the marginal-related O site (0.57 eV, Fig. 3d). Despite this, protons still preferentially adsorb at the N sites rather than the O sites in both Ru-*NO models. These results indicate that the interfacial electron-deficient Ru site facilitates the preferential hydrogenation of the connected N site with a lower energy barrier than the marginal Ru site.

Considering that hydrogen species for the NO_3^-RR hydrogenation process likely originate from adjacent adsorption sites (e.g., Ru sites and O sites in the WO_{3-x}), we calculated the proton adsorption free energy of different Ru and O sites in the initial Ru/WO_{3-x} model. The result shows that the bridged O atom with electron accumulation at the Ru/WO_{3-x} heterointerface possesses the optimal proton adsorption ability. The required free energy (−1.75 eV) is lower than that of the interfacial Ru (−0.4 eV), marginal Ru sites (−0.33 eV), and marginal O atoms (−1.31 eV). The interfacial O sites are expected to facilitate the proton transfer during the NO_3^-RR hydrogenation process.

Proton transfer pathway of the Ru/WO_{3-x} catalyst in acidic NO_3^-RR

To probe the proton adsorption and transfer behavior in the Ru/WO_{3-x} from an electrochemical kinetics perspective, we performed cyclic voltammetry (CV) in 1 M H_2SO_4 and compared it with individual Ru and WO_{3-x} (Fig. 4a). As CV scans from high to low potentials, WO_{3-x} first removes the pre-inserted water molecules[20], followed by proton insertion into the six-membered WO_6 rings between 0.32 and 0 V vs. RHE (with 80% *iR* correction, region #1). As the potential shifts further negative (0 to −0.075 V vs. RHE, region #2), protons are directly inserted in WO_6 cells, and hydrated protons subsequently integrate into the lattice between −0.075 and −0.22 V vs. RHE (region #3). The WO_{3-x} finally undergoes HER once the potential reaches −0.4 V vs. RHE. In contrast, Ru metal shows only a minor Ru^{3+}/Ru redox couple (0.9-0.6 V vs. RHE) and weak proton electro-adsorption between 0.1 and 0 V vs. RHE (region #4)[26]. Notably, both the proton-storage potential window and capacity of Ru are far smaller than those of WO_{3-x}. For the Ru/WO_{3-x}, the proton-insertion region expands significantly (0.9-0.15 V vs. RHE, region #1), and the interval 0.15-0 V vs. RHE likely encompasses simultaneous proton insertion into WO_6 and electro-adsorption on Ru (regions #2 and #4). HER becomes dominant below 0 V vs. RHE. These results highlight that the SMSI in the Ru/WO_{3-x} elevates the proton-insertion potential via interfacial electron-regulated O atoms. Moreover, the Ru/WO_{3-x} exhibits more reversible proton de-insertion/insertion than WO_{3-x}, as reflected by the higher anodic-to-cathodic peak-current ratio in region #1 (0.85 vs. 0.64), a

feature that likely enhances its reverse-hydrogen-spillover capability during NO_3^-RR.

To directly assess proton transfer during NO_3^-RR, we compared transient CV curves (with 80% *iR* correction) in 1 M H_2SO_4 with and without 0.1 M KNO_3 (Fig. 4a). The proton-insertion current of the Ru/WO_{3-x} decreases slightly between 0.6 and 0.3 V vs. RHE in the presence of nitrate, while the subsequent proton de-insertion current is markedly suppressed. This indicates that protons inserted into WO_{3-x} are efficiently consumed by NO_3^-RR via transfer to adjacent Ru sites. To confirm that WO_{3-x}-mediated proton supply is dominant over mere surface processes on Ru, we employed a Li^+-poisoning strategy in 0.05 M H_2SO_4/0.5 M Li_2SO_4 electrolytes. This selectively blocks proton-insertion channels in the WO_{3-x} without passivating Ru sites, leading to a pronounced suppression of both proton-insertion capacity and NO_3^-RR current (Supplementary Fig. 16). The result underscores the critical role of the bulk WO_{3-x} proton reservoir in accelerating reaction kinetics.

We next employed a three-step methodology to systematically verify the reverse-hydrogen-spillover effect. First, steady-state chronopotentiometry at −25 mA cm^{-2} confirmed that proton insertion precedes NO_3^-RR. Similar to the WO_{3-x}, the Ru/WO_{3-x} undergoes a slow proton insertion process and takes approximately 400 s to stabilize in 1 M H_2SO_4 (Supplementary Fig. 17a). In contrast, pure Ru metal exhibits negligible proton electro-adsorption behavior, nearly identical to the CV analysis. Of note, the proton insertion initial potential of the Ru/WO_{3-x} (0.87 V vs. RHE, with 80% *iR* correction) is higher than that of the WO_{3-x} (0.32 V vs. RHE), also consistent with the CV results. We further conducted the same test in 1 M H_2SO_4/0.1 M KNO_3 mixed electrolytes. The result indicates that the Ru/WO_{3-x} continues to exhibit robust proton embedding behavior prior to achieving a stabilized NO_3^-RR potential at around 0.235 V vs. RHE in the hydrogenation potential region #1 (Supplementary Fig. 17b). Chronoamperometry tests further show that proton-insertion capacity increases progressively as the potential shifts from 0.6 to 0 V vs. RHE (without *iR* correction, Supplementary Fig. 18), confirming abundant proton insertion prior to NO_3^-RR. Ex-situ XPS after electrolysis (at −0.3 A cm^{-2} in 1 M H_2SO_4 with and without 0.1 M KNO_3) provides additional evidence. After HER, the W 4*f* spectra shift negatively by 0.2 eV, while after NO_3^-RR they remain nearly unchanged (Supplementary Fig. 19a), suggesting a dynamic equilibrium of proton insertion/de-insertion that preserves the W oxidation state. These observations are further supported by O 1*s* XPS analysis, which reveals distinct oxygen chemical state evolution under different reaction conditions. After the HER, a 0.2 eV downward shift in the O 1*s* peak position is observed, consistent with the formation of W-OH groups through proton insertion (Supplementary Fig. 19b). These hydroxyl species exhibit lower binding energy compared to the dominant oxygen vacancies[23]. In contrast, the O 1*s* spectra remain unchanged after NO_3^-RR, suggesting that the WO_{3-x} serves primarily as a proton relay mediator rather than undergoing permanent chemical modification during NO_3^-RR.

Second, to probe hydrogen spillover, we performed proton insertion/de-insertion experiments. If pre-inserted protons in WO_{3-x} do not participate in NO_3^-RR, the proton-extraction profiles in linear sweep voltammetry (LSV) would be identical with and without nitrate (Fig. 4b). Our experimental results show that the WO_{3-x} undergoes proton insertion between 0.1 (only proton insertion currents) and −0.4 V vs. RHE (along with NO_3^-RR currents, without *iR* correction, Supplementary Figs. 20 and 21), exhibiting proton insertion currents prior to NO_3^-RR onset. This behavior, coupled with the overlap of CV curves in electrolytes with and without nitrate (Fig. 4a), indicates that WO_{3-x} facilitates NO_3^-RR through a continuous proton-coupled electron transfer mechanism rather than via migration of surface pre-inserted protons[27]. In contrast, the Ru/WO_{3-x} exhibits noticeable disparity in proton extraction profiles at 0.6 V vs. RHE in nitrate-containing electrolyte, with increasing intensity as the potential shifts negatively to 0 V vs. RHE (Supplementary Fig. 22). These observations suggest that the inserted protons in the Ru/WO_{3-x} either directly overflow to interfacial Ru-*N sites for NO_3^-RR hydrogenation, or participate in the electroreduction of Ru sites, with the latter requiring substantially less charge. Indeed, the in situ XAS test indicates that the Ru oxidation state and Ru-Ru coordination distance remain unchanged upon the NO_3^-RR with varying applied potentials (without *iR* correction, Supplementary Fig. 23a, b). In addition, post-reaction Ru 3*p* orbital XPS spectra also show no significant changes after both the NO_3^-RR and HER electrolysis (Supplementary Fig. 23c). These results, together with the distinct proton extraction behavior in nitrate-containing and nitrate-free electrolytes, strongly support the hydrogen spillover pathway as the dominant mechanism. We also semi-quantified the hydrogen overflow ratio at various potentials by integrating the positive charge difference from the corresponding LSV curves in two electrolytes. The result shows that the hydrogen overflow proportion increases from 3.75% to 52.07% as the potential decreases from 0.6 to 0 V vs. RHE (Fig. 4c). Simultaneously, the cathodic current density for NO_3^-RR remarkably increases from 0.51 to 100 mA cm^{-2}. Control experiments further demonstrate that the hydrogen overflow ratio increases sensitively with the availability of Ru sites (achieved by increasing the Ru loading amounts) (Supplementary Figs. 24–28).

To evaluate whether this dynamic proton exchange can sustain high-current-density operation, we combined depth-resolved XPS, in situ spectroscopy, and kinetic analysis. Depth-resolved XPS reveals that proton insertion is confined to the near-surface region of the WO_{3-x} support (Supplementary Fig. 29), as evidenced by a progressive shift of the W4*f* binding energy with Ar^+ etching time up to ~8 s, after which the signal stabilizes. This surface-limited protonation facilitates rapid electric-field-driven proton migration to the Ru active sites, consistent with the pseudocapacitive behavior of hexagonal WO_3. The potential-dependent dynamics of proton insertion/de-insertion were further corroborated by in situ XAS (Fig. 4d, e). In pure 1 M H_2SO_4 electrolyte, the W L_3-edge XANES and EXAFS show a gradual reduction of W oxidation states and lengthening of W-O bonds as the potential shifts negatively from 0.3 to 0 V vs. RHE (without *iR* correction), whereas these changes are minimal in the presence of nitrate, indicating that proton insertion and de-insertion reach a fast dynamic equilibrium during NO_3^-RR. We also conducted in situ Raman tests on the Ru/WO_{3-x} in 0.1 M HNO_3. The results indicate that the typical O-W-O stretching vibration exhibits a significant red shift once the Ru/WO_{3-x} was subjected to a fixed potential of 0.6 V vs. RHE (without *iR* correction, Supplementary Fig. 30), which is likely due to the formation of H-O-W-O-H bonds[17,28,29]. As the potential further shifts negatively to 0 V vs. RHE, the corresponding band gradually blue-shifts, returning close to its initial state. This phenomenon is caused by the accelerated reverse hydrogen spillover behavior of the Ru/WO_{3-x}, which is consistent with the results of proton insertion/de-insertion experiments. Notably, we observe that the W-O related vibrational signals gradually weaken with the negative shift of potential. This is because abundant proton insertion triggers the WO_{3-x} support to undergo a semiconductor to metal transition[30], thereby improving the electronic conductivity of the WO_{3-x} support during the acidic NO_3^-RR. To quantify the proton supply capability, we analyzed the chronoamperometric response at 0 V vs. RHE (Supplementary Fig. 31). Kinetic fitting yielded a maximum proton-insertion rate (r_{max}) of 1.82×10^{-5} mol H^+ cm^{-2} s^{-1} in NO_3^--containing electrolyte, which exceeds the NO_3^-RR limiting hydrogenation rate (1.4×10^{-6} mol H^+ cm^{-2} s^{-1}) by more than an order of magnitude (Supplementary Note 1). Moreover, the hydrogen-spillover ratio derived from proton insertion/de-insertion experiments reaches ~52.07% at 0 V vs. RHE (Fig. 4c), corresponding to a proton de-insertion rate of 9.48×10^{-6} mol H^+ cm^{-2} s^{-1}. These values confirm that the proton flux provided by the WO_{3-x} support via reverse hydrogen spillover can readily match the proton demand of NO_3^-RR at a steady-state current

density of −120 mA cm^{-2}. Collectively, the surface-confined proton storage, fast potential-dependent insertion/de-insertion dynamics, and sufficient proton-supply kinetics ensure that the Ru/WO_{3-x} heterostructure maintains a robust proton balance, enabling sustained high-performance NO_3^--to-NH_3 conversion under practical current densities.

Third, for the hydrogenation pathway, we carried out a transition state analysis for the key potential determining step of the interfacial Ru-*NO to the Ru-*NHO hydrogenation pathway. In this process, the involved hydrogen atom originates from either overflowed hydrogen atoms through the WO_{3-x} support or adsorbed hydrogen atoms on adjacent Ru sites. Our DFT calculations provide critical insights into the hydrogen transfer energetics of the Ru/WO_{3-x}. While the interfacial proton transfer pathway exhibits a substantial energy barrier of 4.06 eV (Fig. 4f), it remains thermodynamically favorable compared to hydrogen migration between surface Ru atoms (4.28 eV, Fig. 4f). More significantly, we identified multiple lower-barrier pathways (0.83–2.65 eV, Supplementary Fig. 32) for near surface intercalated hydrogen spillover, suggesting that proton transfer through WO_{3-x} subsurface layers dominates the hydrogen delivery mechanism. These computational results strongly support our experimental observations, revealing that the WO_{3-x} support not only serves as a proton reservoir but also provides energetically favorable pathways for hydrogen transport to the active Ru sites. We further performed ^2H (i.e., D) isotope-labelled experiments to validate this inference. Specifically, we introduced D into the Ru/WO_{3-x} using 1 M D_2SO_4 as electrolyte at 0.2 and 0 V vs. RHE (without *iR* correction), respectively, followed by the NO_3^-RR electrocatalysis at 0 V vs. RHE in 1 M H_2SO_4/0.1 M KNO_3. Alongside the normal intermediates (Supplementary Fig. 33), we detected extra ND_2OH (mass-to-charge ratio, m/z = 35) and ND_2H (m/z = 19) species (Fig. 4g). This demonstrates that D stored in the WO_{3-x} can migrate to interfacial Ru-*NO sites for further hydrogenation. Whereas the absence of ND_2OD (m/z = 36) or ND_3 (m/z = 20) suggests that hydrogen species hydrogenated at the O sites of the *NDO and the final N sites of the *ND_2 directly originate from protons in the electrolyte. Indeed, the NO_3^-RR free energy diagram indicates that both steps are thermodynamically spontaneous reactions, distinct from the hydrogenation steps of *NO to *NHO and *NHOH to *NH_2OH (Fig. 3b, Supplementary Table 1). To gain atomic-level insight, we employed Ab initio molecular dynamics (AIMD) simulations to investigate the interactions between protons in the electrolyte and the interfacial Ru-*NHO model (Supplementary Data 1). The results demonstrate that one proton would spontaneously bond with the O atom in the model, achieving a stable atomic distance of ~1 Å (Fig. 4h). In contrast, another dissociative proton initially near the N site gradually migrates away, exhibiting behavior distinct from a stable N-H bond (Supplementary Fig. 34). These simulations further confirms that the protons from the electrolytes, in addition to those stored in the WO_{3-x} support, can directly participate in NO_3^-RR hydrogenation process.

Integrating these findings, we establish that the electro-deficient Ru sites at the Ru/WO_{3-x} heterointerface promote an upshift of the N 2*p* band center, thermodynamically facilitating the hydrogenation of Ru-*NO intermediate (i.e., the potential-determining step) during NO_3^-RR. The hydrogen supply is ensured by a triple pathway: pre-inserted protons in WO_{3-x} delivered via reverse hydrogen spillover, interfacial adsorbed protons, and protons directly captured from the electrolyte. This multi-source proton-supply strategy, coupled with a dynamic proton insertion/de-insertion equilibrium that sustains high current densities, underpins the exceptional acidic NO_3^-RR performance of the Ru/WO_{3-x}.

Acidic NO_3^-RR performance analysis of the Ru/WO_{3-x} catalyst

To highlight the SMSI advantages (specifically, the modulated electronic structure and unique reverse hydrogen spillover ability) of the Ru/WO_{3-x} heterostructure over individual Ru and WO_{3-x} components, we then conducted the acidic NO_3^-RR measurements in 1 M H_2SO_4/0.1 M KNO_3 mixed electrolytes, whose preparation method is described in Supplementary Note 2. The three-electrode measurements were carried out in a standard H-type electrolytic cell, and the Hg/Hg_2SO_4 reference electrode potential was calibrated by HER and hydrogen oxidation reaction CV curves using Pt as both the working and countering electrodes (Supplementary Fig. 35)[31]. Geometric polarization curves with 80% *iR* correction were recorded by steady-state chronopotentiometry with electrolyte stirring to avoid mass transfer interference. A typical example of the Ru/WO_{3-x} is shown in Supplementary Fig. 36. Geometric polarization curves reveal that the Ru/WO_{3-x} exhibits optimal NO_3^-RR activity, achieving 0.168 V vs. RHE at −100 mA cm^{-2}, significantly higher than that of the Ru (−0.028 V vs. RHE) and WO_{3-x} (−0.438 V vs. RHE, Fig. 5a). Notably, the Ru/WO_{3-x} maintains a positive potential of 0.026 V vs. RHE even at −500 mA cm^{-2}, effectively excluding the potential possibility of competing HER. Further improvements in the geometric activity of the Ru/WO_{3-x} were achieved by adjusting the mass transfer of reactants. For instance, increasing the nitrate concentration in the electrolyte from 0.1 to 1 M leads to a remarkable rise in potential from -0.013 to 0.101 V vs. RHE at −600 mA cm^{-2} (Supplementary Fig. 37). We further systematically investigated the effect of Ru loading on catalytic performance by synthesizing three Ru/WO_{3-x} catalysts with controlled Ru loadings through precise adjustment of Ru precursor concentrations. The result suggests a significant enhancement in NO_3^-RR activity when increasing Ru loading from 0.42 to 0.98 mg cm^{-2}, while further increasing to 1.12 mg cm^{-2} shows negligible improvement (Supplementary Fig. 28 and 38), establishing 0.98 mg cm^{-2} as the optimal loading that balances cost and performance. We further measured the electrochemically active surface area (ECSA) of Ru using a reported Cu underpotential deposition/stripping protocol[26] (Supplementary Figs. 39, 40). The polarization curves normalized by Ru ECSA are nearly identical (Supplementary Fig. 41). This indicates that while variations in Ru loading affect the ECSA and thus the apparent activity, they have a negligible impact on the intrinsic activity. In contrast, the Ru ECSA- or mass-normalized polarization curves reveal that the Ru/WO_{3-x} catalyst exhibits significantly higher catalytic activity than Ru alone (Supplementary Fig. 42), underscoring the advantages of the SMSI effect between Ru and the WO_{3-x} support.

The accelerated NO_3^-RR hydrogenation kinetics of the Ru/WO_{3-x} was evaluated using Tafel plot derived from geometric polarization curves in the low-current region, avoiding interference from HER and mass transfer. The Ru/WO_{3-x} exhibits a small Tafel slope (97 mV dec^{-1}), much lower than that of the Ru (175 mV dec^{-1}) and WO_{3-x} (322 mV dec–^{1}, Fig. 5b). Electrochemical impedance spectroscopy (EIS) was also used to evaluate initial proton insertion kinetics and subsequent NO_3^-RR hydrogenation kinetics at a fixed potential of 0.2 V vs. RHE (without *iR* correction, the simulated equivalent circuit diagram is shown in Supplementary Fig. 43). Nyquist spectra indicate that the Ru/WO_{3-x} possesses both the lower proton insertion and NO_3^-RR hydrogenation resistances (0.05 and 2.44 Ω, respectively) than the Ru metal (12.36 and 16.65 Ω, respectively), while the WO_{3-x} only exhibits the surface-controlled pseudocapacitive behavior of proton insertion (Fig. 5c and Supplementary Table 2). In summary, the enhanced NO_3^-RR activity (both the reaction potential and hydrogenation kinetics) of the Ru/WO_{3-x} compared to the Ru metal possibly originates from the interfacial electron-deficient Ru sites and the unique reverse hydrogen spillover behavior triggered by the SMSI effect, as discussed earlier (Fig. 3 and Fig. 4). We also found that the WO_{3-x}-mediated reverse hydrogen spillover behavior can enhance the acidic HER activity. The Ru/WO_{3-x} exhibits higher geometric activity, Ru mass- and ECSA-normalized activity, as well as lower Tafel slope than the Ru catalyst (Supplementary Fig. 44), well in line with the previous report[17].

https://doi.org/10.1038/s41467-026-69335-x

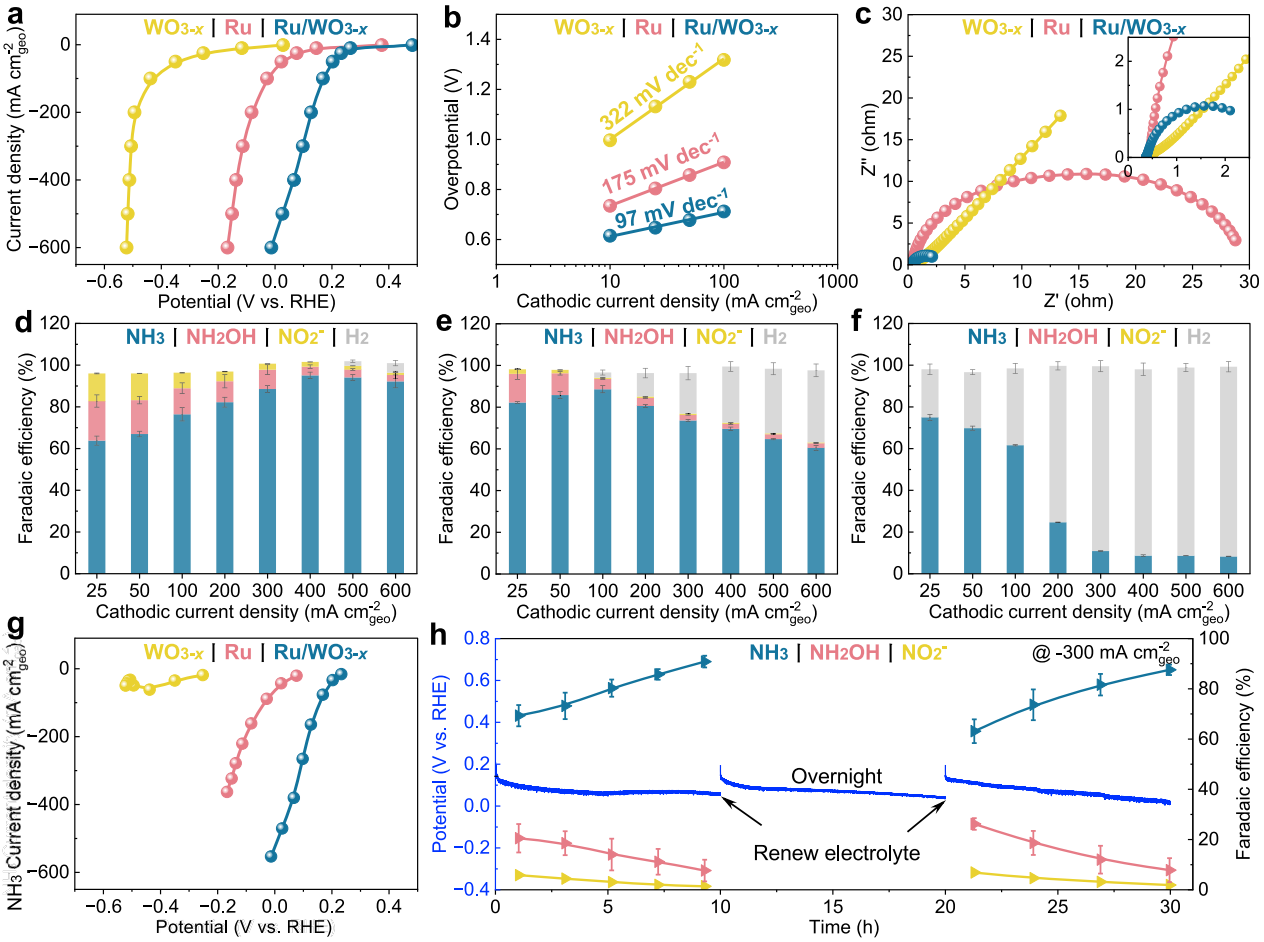

Fig. 5 | Acidic NO3-RR performance. a Geometric polarization curves, (**b**) Tafel plots and (**c**) Nyquist plots of Ru/WO_{3-x}, Ru and WO_{3-x}. Faradaic efficiency plots of (**d**) Ru/WO_{3-x}, (**e**) Ru and (**f**) WO_{3-x} at different cathodic current densities. **g** NH_3 Faradaic efficiency normalized polarization curves. **h** Chronopotentiometry curves and corresponding Faradaic efficiency for Ru/WO_{3-x} at −300 mA cm^{-2}. Faradaic efficiency data represent the average of three independent experiments (**d**–**f** and **h**). All potentials in (**a**), (**b**), (**g**) and (**h**) are *iR*-corrected by 80%. Source data for Fig. 5 are provided as a Source Data file.

We then examine the NO_3^-RR Faradaic efficiencies of the three catalysts using chronopotentiometry at fixed charges of 1440 C. Subsequently, we quantified the NO_2^-, NH_2OH, and NH_3 products in the electrolyte using ion chromatography (IC) and ultraviolet-visible (UV-Vis) spectrophotometry (Supplementary Fig. 45–47). Specifically, the NO_2^- and NH_2OH Faradaic efficiencies of the Ru/WO_{3-x} decline gradually (from 13.21% to 1.09% and from 18.99% to 3.09%, respectively) as the current densities ranged from −25 to −600 mA cm^{-2} (Fig. 5d). In contrast, NH_3 Faradaic efficiencies rapidly increase from 63.79% to a maximum of 95.08% at −400 mA cm^{-2}, and then slowly reduce to 94.09% and 92.19% at −500 and -600 mA cm^{-2}, respectively. The initial increase in the NH_3 Faradaic efficiency is attributed to the potential-dependent NO_3^-RR hydrogenation process, while the subsequent slight decline results from the competing HER. Indeed, the NO_3^-RR polarization curve of the Ru/WO_{3-x} is close to the HER counterpart at high cathodic current densities (Supplementary Fig. 48a). Notably, the NO_3^-RR hydrogenation efficiency of the Ru/WO_{3-x} highly relies on the reverse hydrogen spillover degree controlled by applied potential or current densities, as revealed by the proton insertion/de-insertion experiment (Fig. 4c). Similarly, the NH_3 Faradaic efficiencies of the Ru metal also exhibit an upward and then downward trend with a peak value of 88.58% at −100 mA cm^{-2} (Fig. 5e). However, Ru metal suffers from severe HER side reaction at higher cathodic current densities due to the more favorable HER kinetics than NO_3^-RR (Supplementary Fig. 48b). Compared to the Ru/WO_{3-x} and Ru, the WO_{3-x} selectively promotes NO_3^-RR towards NH_3 aqueous product (Fig. 5f), likely because it conducts a $9H^+/8e^-$ proton-coupled electron transfer process without surface hydrogen transfer[27], as revealed by the overlapped CV reverse sweep curves as well as proton insertion/de-insertion experiments (Fig. 4a, Supplementary Figs. 20 and 21). Similarly, the NH_3 Faradaic efficiencies are influenced by the competing HER as the cathodic current densities increase (Supplementary Fig. 48c). In addition to the Faradaic efficiency analysis, we also calculated the corresponding yield rates for the NO_2^-, NH_2OH and NH_3 products. The NH_3 yield rates increase rapidly with rising cathodic current densities for the Ru/WO_{3-x} and Ru, while the WO_{3-x} reaches a plateau (Supplementary Fig. 49). The NO_2^- and NH_2OH yield rates remain relatively unchanged for the Ru/WO_{3-x} and Ru due to the accelerated hydrogenation kinetics. Notably, N_2H_4 was not detected in the electrolyte after the NO_3^-RR of the three catalysts (Supplementary Fig. 50), thereby ruling out the dual-N sites coupling reaction pathway.

To precisely identify the NO_3^-RR geometric activity of the three catalysts towards the NH_3 targeted product, we normalized the geometric current density by NH_3 Faradaic efficiencies. Polarization curves indicate that the Ru/WO_{3-x} still possesses the highest geometric activity for NH_3 production (Fig. 5g). This performance is competitive with other recently reported high-performance acidic NO_3^-RR catalysts (Supplementary Table 3)[32–37]. It is noted that these state-of-the-art catalysts could not reach a higher NO_3^-RR cathodic current density than 200 mA cm^{-2} for NH_3 production due to the competing HER,

while our designed Ru/WO_{3-x} avoids the issue by geometrical separation of hydrogen and nitrate adsorption sites and subsequent potential-regulated reverse hydrogen spillover way.

Previously studies have shown that TiO_{2-x} with oxygen vacancies exhibits certain NO_3^-RR performance towards ammonia[36,38]. To investigate this, we subjected the titanium felt substrate to reductive calcination and measured its acidic NO_3^-RR performance. The result reveals nearly identical NO_3^-RR and HER activity (Supplementary Fig. 51). The maximum NH_3 Faradaic efficiency is 11.94% at −25 mA cm^{-2}, gradually decreasing to 3.85% as cathodic current density increases to −600 mA cm^{-2}. NO_2^- Faradaic efficiencies remain consistently below 0.5%, and no NH_2OH is detected. These results demonstrate that the titanium felt has limited NO_3^-RR performance, thus is less likely to largely impact the NO_3^-RR performance of the three catalysts.

To mitigate interference from environmental ammonia species, we conducted acidic NO_3^-RR measurements on the Ru/WO_{3-x} in ^{15}N isotope labelled nitrate electrolytes at −200 mA cm^{-2}. The ^1H nuclear magnetic resonance (NMR) spectra indicate that the ratio of the integral area of the $^{15}NH_4^+$ doublet to the hydroquinone singlet is ca. 12.41:1, nearly identical to that of the $^{14}NH_4^+$ triplet to the hydroquinone singlet (12.42:1, Supplementary Fig. 52). The calculated NH_4^+ Faradaic efficiencies based on the NMR spectra closely matches those determined by IC (ca. 83.2% and ca. 82.5%, respectively), confirming the absence of interference from environmental ammonia species.

Additionally, we assessed the NO_3^-RR stability of the Ru/WO_{3-x} at -300 mA cm^{-2}. Higher current densities would challenge the operation stability (Supplementary Fig. 53). The chronopotentiometry curves exhibit a slight potential decline with prolonged reaction time or accumulated nitrate consumption (Fig. 5h). However, renewing the electrolytes restores the potential, implying that the mass transfer rate of the reactant also influences the NO_3^-RR stability. This observation aligns with the nitrate concentration-dependent polarization curves (Supplementary Fig. 37). During the electrolysis, the NO_2^- and NH_2OH Faradaic efficiencies decrease from ca. 6% and 22% to ca. 2% and 8%, respectively. In contrast, the NH_3 Faradaic efficiencies instead increase from ca. 65% to 90%. These findings suggest that the NO_3^-RR hydrogenation efficiency of the Ru/WO_{3-x} is also affected by reactant concentrations in the electrolyte.

To verify the above supposition, we performed the acidic NO_3^-RR measurements in 0.5 M and 1 M nitrate electrolytes. The Faradaic efficiencies of NO_2^- and NH_2OH intermediates significantly improve, while the final NH_3 Faradaic efficiencies are restricted with the increase in nitrate-enriched concentrations at the same cathodic current density (Supplementary Fig. 54). This implies that higher reactant concentrations would inhibit the NO_3^-RR hydrogenation process likely due to the limited hydrogen supply at the fixed charges. Interestingly, NO_2^- and NH_2OH Faradaic efficiencies exhibit a gradual decline trend, while NH_3 Faradaic efficiencies increase gradually with rising cathodic current densities in the electrolytes with the same nitrate concentration. This suggests that the increasing cathodic current densities or lowering potential still promotes the NO_3^-RR hydrogenation process through the reverse hydrogen spillover effect. It is noted that the Ru/WO_{3-x} can operate steadily at an industrial level current density of −500 mA cm^{-2} for at least 100 h in 1 M H_2SO_4/1 M KNO_3, achieving a final NH_3 Faradaic efficiency of ca. 88% (Supplementary Fig. 55).

Post-reaction characterizations of the Ru/WO_{3-x} reveal consistent Ru 3*p*, W 4*f*, and O 1*s* orbital XPS spectra before and after the electrocatalysis (Supplementary Fig. 19, 23c). Notably, the N 1*s* orbital XPS spectra do not show any signal enhancement on the catalyst surface (Supplementary Fig. 56a), suggesting no nitride generation. XRD patterns exhibit diffraction peaks corresponding to both the Ru and WO_{3-x} with the typical hcp structure (Supplementary Fig. 56b). Raman spectra display consistent band signals, reflecting unchanged electronic structure (Supplementary Fig. 56c). SEM image depicts dense and cross-growth of the Ru/WO_{3-x} on the titanium felt (Supplementary Fig. 56d). Additionally, the HAADF-STEM image and the corresponding elemental maps still highlight edge-enriched Ru nanoparticles on the WO_{3-x} surface (Supplementary Fig. 56e). The HRTEM image also shows a heterointerface boundary between Ru (100) and WO_{3-x} (002) planes (Supplementary Fig. 56f). Based on these post-physical characterizations, we conclude that the Ru/WO_{3-x} did not undergo significant structural changes during NO_3^-RR.

Performance analysis of the sulfide-nitrate "batterolyzer"

For practical application, we assembled an electrochemical cell by coupling anodic alkaline S^{2-}OR with cathodic acidic NO_3^-RR. Here we coined the term "batterolyzer" for this type of electrochemical cell, which can generate electricity like a battery, and at the same time produce high-value chemicals like an electrolyzer (Fig. 6a). The needle-like Co_9S_8 catalyst was prepared for the alkaline S^{2-}OR (Supplementary Fig. 57)[39]. The catalyst requires 0.35 V vs. RHE or -0.479 V vs. SHE to reach 300 mA cm^{-2} and operates steadily for at least 30 h in 1 M NaOH/1 M Na_2S mixed electrolytes (Supplementary Fig. 58). Without electric driving force, the open circuit voltage of the assembled batterolyzer gradually declines from initial ca. 1.25 to 0.97 V at 2000 s due to the spontaneous acid-base neutralization through proton exchange membranes (Fig. 6b). The batterolyzer achieves a peak discharge power density of 39.4 mW cm^{-2} when the current density reaches 100 mA cm^{-2} at 298 K (without *iR* correction, Fig. 6c). If the device is further heated to 353 K using low-grade thermal energy from industry, the peak discharge power density can further increase to 43.4 mW cm^{-2}, which is competitive with many other pollutant-type devices, such as zinc-nitrate[40–43], urea-nitrate[44], hydrazine-nitrate[36,45], zinc-nitric oxide[46–49], and formaldehyde-nitrate batterolyzers[50] (Supplementary Table 4). Notably, using zinc foil as sacrificial anodes for a power supply is not recommended due to the potential increases in operating costs. Further, coupling the hydrazine oxidation reaction and NO_3^-RR for pollutant batteries is unsustainable, as industrial emissions of hydrazine wastewater are not comparable to nitrate effluent. The produced ammonium nitrate can be further extracted to magnesium ammonium phosphate slow-release fertilizer by the coprecipitation method (Supplementary Fig. 59)[41], while the generated polysulfide can be further thermo-catalyzed to thiosulfate by NiS_x powder[51].

Discussion

In summary, we developed a corrosion-resistant Ru/WO_{3-x} catalyst for acidic NO_3^-RR towards ammonium production. The loaded Ru metal electro-adsorbs nitrate, while the WO_{3-x} support with high proton uptake preferably inserts protons. The intrinsically low HER activity of the WO_{3-x} further ensures the reverse hydrogen spillover from the WO_{3-x} to Ru. This geometrically separated proton and nitrate adsorption configuration not only reduces competing HER kinetics, but also accelerates the nitrate hydrogenation process. Consequently, the Ru/WO_{3-x} delivers a high current density of −500 mA cm^{-2} at a positive potential of 0.026 V vs. RHE in 1 M H_2SO_4/0.1 M KNO_3, along with an ammonia Faradaic efficiency of 94.09%. For practical application, the assembled sulfide-nitrate "batterolyzer" using the Ru/WO_{3-x} as the cathode and Co_9S_8 as the anode achieves a high peak discharge power density of 43.4 mW cm^{-2}, concurrently purifying nitrate and sulfide effluents as well as producing high-value magnesium ammonium phosphate and thiosulfate. This work demonstrates a rational catalyst design strategy by decoupling the regulation of adsorption sites from hydrogen supply. It firmly establishes the efficacy of the WO_{3-x}-mediated reverse hydrogen spillover for acidic NO_3^-RR hydrogenation. This design concept is expected to be extended to other catalytic systems by judiciously balancing key support properties, such as conductivity, hydrogen storage capacity, and pH compatibility, for complex hydrogenation reactions beyond NO_3^-RR.

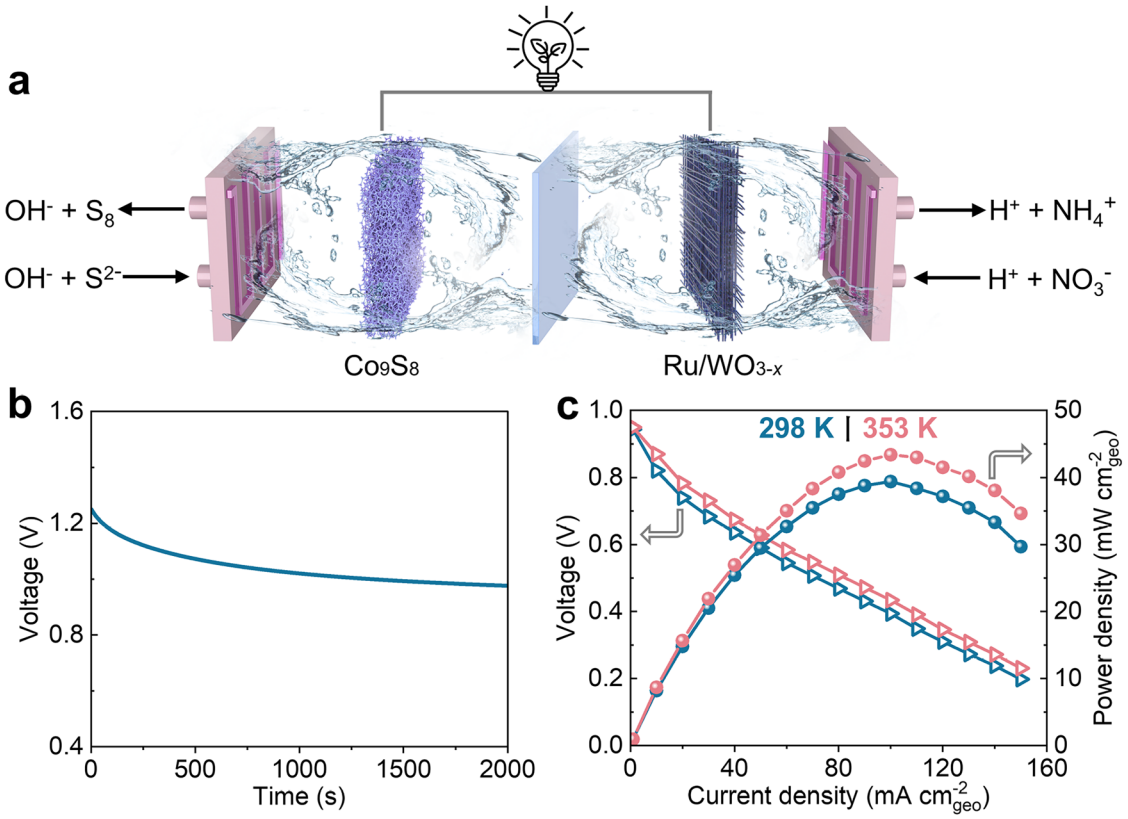

Fig. 6 | Performance of the sulfide-nitrate batterolyzer. a Schematic illustration of the batterolyzer configuration. **b** Open-circuit voltage curve. **c** Polarization and corresponding discharging power density curves. All potentials are not *iR*-corrected. Source data for Fig. 6 are provided as a Source Data file.

Methods

Materials

Hydrochloric acid (HCl, 36-38%), nitric acid (HNO_3, 65-68%), sulfuric acid (H_2SO_4, 95-98%), phosphoric acid (H_3PO_4, 85%), oxalic acid ($H_2C_2O_4$, 99%), ammonium sulfate [$(NH_4)_2SO_4$, 99.9%], cobalt nitrate hexahydrate [$Co(NO_3)_2{\cdot}6H_2O$, 99.99%], ammonium fluoride (NH_4F, 98%), urea (CH_4N_2O, 99%), copper sulfate pentahydrate ($CuSO_4{\cdot}5H_2O$, 99.9%), potassium nitrate (KNO_3, 99%), sodium hydroxide (NaOH, 99.9%), potassium hydroxide (KOH, 85%), dipotassium phosphate (K_2HPO_4, 99%), potassium dihydrogen phosphate (KH_2PO_4, 99%), sodium carbonate (Na_2CO_3, 99.9%) and sodium bicarbonate ($NaHCO_3$, 99.9%) ware purchased from Sinopharm Chemical Reagent Co., Ltd. Hydrated ruthenium trichloride ($RuCl_3{\cdot}xH_2O$, 42-45%), sodium sulfide nonahydrate ($Na_2S{\cdot}9H_2O$, 98%), sodium tungstate dihydrate ($Na_2WO_4{\cdot}2H_2O$, 99.5%), ^{15}N isotope label potassium nitrate (KNO_3, 98.5%) and hydroquinone ($C_6H_6O_2$, 99%) were purchased from Shanghai Maclin Biochemical Technology Co., Ltd. Ammonium (NH_4^+, 100%), hydroxylamine hydrochloride ($NH_2OH{\cdot}HCl$, 100%), hydrazine (N_2H_4, 100%) and nitrite (NO_2^-, 100%) standard solution, trichloroacetic acid (99%), 8-quinolinol (95%), p-dimethylaminobenzaldehyde (99%) and deuterated dimethylsulfoxide (DMSO, 99%) were purchased from Shanghai Aladdin Biochemical Technology Co., Ltd. Dupont N115 proton exchange membrane (PEM, 127 μm thickness), nickel foam (96% porosity, 1 mm thickness) and titanium felt (50-60% porosity, 0.4 mm thickness) were purchased from Suzhou Sinero Technology Co. Ltd. Electrochemical equipment was purchased from Shanghai Yue magnetic electronic Technology Co., LTD and Changsha Spring New Energy Technology Co., Ltd.

Catalyst synthesis

Preparation of Ru/WO_{3-x} on titanium felt. The Ru/WO_{3-x} nanorods self-supported on titanium felt were synthesized by a combination method of hydrothermal treatment[52,53], cation adsorption, and calcination in sequence. To be specific, the hydrothermal solution was first prepared by dissolving 8.2 g $Na_2WO_4{\cdot}2H_2O$ in 300 mL of distilled water, whose pH was then adjusted to 1 by concentrated HCl. Afterwards, $H_2C_2O_4$ aqueous solution (6.3 g, 200 mL) and ammonium sulfate (25 g) were poured into the above solution in sequence. After evenly stirring, 30 mL solution was transferred into an autoclave with the addition of two pieces of pretreated titanium felts (1 cm × 2 cm, which was ultrasonically pre-cleaned in acetone and 3 M HCl for respective 15 min) and maintained at 180 °C for 16 h. After the reaction cooled down, the hydrated $(NH_4)_xWO_3$ precursor self-supported on titanium felt was washed with distilled water and dried under an infrared baking lamp for subsequent use. The cation adsorption was conducted in a sealed glass bottle with the addition of $RuCl_3{\cdot}xH_2O$ aqueous solution (60 mg, 60 mL). Four pieces of $(NH_4)_xWO_3$ precursor on titanium felt were then vertically immersed in the solution under vigorous stirring at 60 °C for 12 h. After the reaction, the Ru species loaded WO_3 precursor on titanium felt was washed by distilled water, dried under an infrared baking lamp, and finally calcined at 400 °C for 4 h under the atmosphere of 10% H_2/Ar mixed gases to form the final Ru/WO_{3-x} heterostructure. The mass loading of Ru and W metals was ca. 0.98 and 7.5 mg cm^{-2}, respectively, determined by a combination method of microwave digestion and inductively coupled plasma optical emission spectrometer (ICP-OES).

Preparation of Ru on titanium felt. $RuCl_3{\cdot}xH_2O$ aqueous solution (13 mg, 130 μL) was ultrasonically mixed with an equal volume of ethanol, both of which were dropped onto the pre-treated titanium felt (1 cm × 2 cm) under ian nfrared baking lamp. The obtained titanium felt was then calcined at 400 °C for 4 h under an atmosphere of 10% H_2/Ar mixed gases to form the Ru metal nanoparticles. The mass loading of Ru is ca. 3 mg cm^{-2}.

Preparation of WO_{3-x} on titanium felt. The WO_{3-x} on titanium felt was synthesized by calcining the hydrated $(NH_4)_xWO_3$ precursor at 400 °C for 4 h under the atmosphere of 10% H_2/Ar mixed gases.

Preparation of TiO_{2-x} on titanium felt. The pretreated titanium felt was directly calcined at 400 °C for 4 h under the atmosphere of 10% H_2/Ar mixed gases to form the TiO_{2-x}.

Preparation of Co_9S_8 on nickel foam. The Co_9S_8 nanoneedles on nickel foam were synthesized by two steps of continuous hydrothermal methods[39]. To be specific, the first hydrothermal solution was prepared by dissolving 2 mmol $Co(NO_3)_2{\cdot}6H_2O$, 3 mmol NH_4F, and 8 mmol urea in 30 mL of distilled water. The solution was then transferred into an autoclave with the addition of one piece of pretreated nickel foam (3 cm × 3 cm, which had been ultrasonically cleaned in acetone and 3 M HCl for 15 min) and maintained at 120 °C for 3 h. After the reaction cooled down, the F-doped $Co(OH)_2$ nanoneedle precursor self-supported on nickel foam was washed by distilled water and dried under an infrared baking lamp. The Co_9S_8 nanoneedles were subsequently synthesized by the second hydrothermal treatment of the obtained precursor in $Na_2S{\cdot}9H_2O$ aqueous (10 mmol, 30 mL) under the same reaction conditions.

Physical characterizations

A ZEISS Sigma microscope was used to shoot the SEM images at an acceleration voltage of 15 kV. A FEI Philips Tecnai F30 was used to shoot the TEM, HAADF-STEM, and EDS images at an acceleration voltage of 300 kV. A Rigaku Ultima-IV XRD diffractometer with Cu Kα radiation (λ = 1.5405 Å) was used to record the XRD patterns at a scan rate of 2° min^{-1}. Powder stripped from titanium felt was used for XRD and TEM measurements. A Thermo Scientific Escalab250Xi spectroscope with Al-Kα radiation was used to collect the XPS spectra, wherein C 1s orbit was calibrated to 284.8 eV. A Renishaw inVia confocal Raman microscope was used to record the Raman spectra under an excitation of 532 nm laser with a power of 1 mW. In situ Raman in 0.1 M HNO_3 was conducted using the same laser with a power of 10 mW. Metrohm 850 professional IC was used to quantify the ammonium and nitrite. A Brucker Avance III (500 MHz) was used to collect the ^1H NMR spectra. A Shimadzu UV2550 UV-Vis spectrophotometer, equipped with colorimetric methods, was used to quantify the hydrazine and hydroxylamine. A Shanghai Linglu QAS100 online DEMS was used to explore the potential NO_3^-RR pathway, wherein a water-proof polytetrafluoroethylene membrane with ≥50% porosity, ≤20 nm pore diameter, and 40 μm thickness was used to separate electrolytic from the mass spectrometer system. A simulated configuration can be seen in Supplementary Fig. 13. Ru K-edge and W L_3-edge XAS were conducted at the TPS 44 A beamline of the National Synchrotron Radiation Research Center in Hsinchu. The XAS spectra were acquired using the Quick-EXAFS mode in transmission, capturing both XANES and EXAFS data. Metallic Ru and W foils were employed as references for energy scale calibration. In-situ XAS measurements were conducted in 1 M H_2SO_4 with and without 0.1 M KNO_3 under various applied potentials. EXAFS analysis was performed using Athena software, applying a k^2-weighted transformation to the XAS spectra to assess oscillation changes in k-space. Furthermore, the Fourier transformation was employed to examine R-space, enabling detailed analysis of bond length trends under different bias conditions.

Electrochemical measurements

All the electrochemical measurements were conducted at 298 K on a CHI 660E electrochemical workstation, equipped with a CHI 680 C current amplifier (Shanghai Chenhua Instrument Co., LTD). The acidic NO_3^-RR was measured by a standard three-electrode system in a H-type electrolytic cell, wherein catholyte was 1 M H_2SO_4 and 0.1 M KNO_3 mixed solution (50 mL, pH close to 0) and anolyte was 1 M H_2SO_4 (50 mL, pH close to 0). They were separated by Dupont N115 PEM (without pre-treatment for use). The self-supported catalysts (1 cm × 1 cm), a Pt sheet (1 cm × 1 cm), and Hg/Hg_2SO_4 were used as working, counter and reference electrodes, respectively. The potentials with regard to Hg/Hg_2SO_4 were converted to RHE by a typical CV method in H_2-saturated electrolytes at 1 mV s^{-1} [31]. R_s between working and reference electrodes, determined by EIS at open circuit potentials, is ca. 0.4 Ω in the test system.

NO_3^-RR performance tests. Steady-state chronopotentiometry was used to plot the polarization curves and evaluate the stability (with 80% *iR* correction), where the electrolytes were vigorously stirred at 1000 rpm. In order to avoid the rapid consumption of nitrate through the stability test, the electrode area was reduced to 0.5 × 0.5 cm, and the electrolyte volume increased to 70 mL, wherein R_s increased to ca. 1.1 Ω. Tafel plots were obtained by the transformation of geometric polarization curves to evaluate NO_3^-RR hydrogenation kinetics according to the following equation.

$$\eta = a + b \times logj \tag{1}$$

wherein η, a, b and j were the overpotential of NO_3^-RR, exchange current density, Tafel slope and current density, respectively. EIS was also performed at a fixed potential of 0.2 V vs. RHE (without *iR* correction) with frequency range from 10^5 to 0.01 Hz and an amplitude of 5 mV. After constant-current electrolysis at fixed charges of 1440 C, the NO_3^-RR product was quantified, and the corresponding Faradaic efficiency was calculated according to the following equation.

$$\text{Faradaic efficiency} = nzF/It \tag{2}$$

wherein n, z, F, I and t is molar mass of product (mol), electron transfer number, the Faradaic constant (96485 C mol^{-1}), current (A) and time (s), respectively.

Hydrogen spillover tests. CV was first employed to explore the proton (de)insertion potentials of the investigated catalysts in 1 M H_2SO_4 with or without nitrate. Continuous pre-activation process was conducted at 10 mV s^{-1} until the catalysts stabilize. Proton insertion/deinsertion (Eq. 3) measurements were then used to decide whether the protons that were pre-inserted in WO_{3-x} participated in NO_3^-RR and further calculate the hydrogen spillover percentage.

$$WO_{3-x} + xH^+ + xe^- \rightarrow H_xWO_{3-x} \tag{3}$$

To be specific, chronoamperometry at fixed potentials (0-0.6 V vs. RHE with sampling interval of 0.1 V, without *iR* correction) for continuous 200 s was first employed to insert protons from electrolytes into WO_{3-x}, and LSV curves at 10 mV s^{-1} from the same fixed potential to final 0.8 V vs. RHE were then recorded to estimate the peak area of proton desorption. During the measurement, the electrolyte was macroscopically static without stirring. By integrating the corresponding peak area difference in 1 M H_2SO_4 with or without 0.1 M KNO_3, the overflowed hydrogen, whether for the participation in NO_3^-RR can thus be identified and the corresponding percentage can be further calculated.

Isotope labeled DEMS tests. In order to further identify whether the overflowed hydrogen participated in the NO_3^-RR, we carried out ^2H (i.e., D) isotope-labeled NO_3^-RR experiments via online DEMS. To be specific, D was first inserted into the Ru/WO_{3-x} in 1 M D_2SO_4 in a custom-made electrolytic cell by chronoamperometry fixed at 0 V or 0.2 V vs. RHE (without *iR* correction) for 120 s, respectively ($R_s \approx 3.8$ Ω). After the cell was thoroughly rinsed and dried to remove the residual D_2SO_4 electrolyte, 1 M H_2SO_4/0.1 M KNO_3 mixed electrolytes were injected into the cell. The NO_3^-RR tests were subsequently conducted by chronoamperometry fixed at 0 V vs. RHE (without *iR* correction) for intermittent 120 s, and meanwhile, the obtained reaction products containing D can be immediately speculated by mass-to-charge ratio analysis.

Cu underpotential deposition/stripping tests. Cu underpotential deposition/stripping (Eq. 4) measurements were used to determine the ECSA of Ru atoms in the Ru/WO_{3-x} and Ru electrodes[26].

$$Cu^{2+} + 2e^- \rightarrow Cu \quad (4)$$

To be specific, chronoamperometry at a fixed potential of 0.3 V vs. RHE (without *iR* correction) for continuous 200 s was first employed to deposit Cu atoms on the surface of Ru metal sites in a 1 M H_2SO_4, and 2 mM $CuSO_4$ mixed electrolyte, and the LSV curves at 10 mV s^{-1} from 0.3 to 0.8 V vs. RHE were then recorded to estimate the desorption peak area of the deposited Cu atoms. By integrating the corresponding peak areas in 1 M H_2SO_4 with or without 2 mM $CuSO_4$, the stripping charge of the deposited Cu can thus be calculated. Cu metal was theoretically deposited in the form of a monoatomic layer on the surface of Ru metal, and the ECSA of the Ru/WO_{3-x} and Ru electrodes can thus be calculated by the stripping charge dividing the theoretical monolayer deposition charge (420 μC cm^{-2}).

HER test. HER was conducted at the same protocol except that the catholyte was replaced with 1 M H_2SO_4.

Sulfide oxidation reaction test. S^{2-}OR was conducted at the same protocol except that the catholyte and anolyte were replaced with 1 M NaOH and 1 M NaOH/1 M Na_2S electrolytes, respectively. The reference electrode was also substituted with a pristine Hg/HgO electrode, and the potentials were converted to RHE by Nernst equation as follows.

$$E_{RHE} = E_{Hg/HgO} + 0.098 + 0.0592*pH - 80\%iR \quad (5)$$

wherein the pH of electrolytes was measured by acidometer.

Sulfide-nitric acid batterolyzer tests. The sulfide-nitric acid batterolyzer was assembled in a membrane electrode assembly flow reactor, wherein one piece of Co_9S_8 on nickel foam (2 cm × 2 cm) and one piece of Ru/WO_{3-x} on titanium felt (2 cm × 2 cm) were used as anode and cathode, respectively. Anolyte was 1 M NaOH/1 M Na_2S mixed electrolyte while catholyte was 1 M H_2SO_4/0.1 M KNO_3 mixed electrolyte. They were separated by a Dupont N115 PEM (without pre-treatment) and circularly flowed at a rate of 150 mL min^{-1} by peristaltic pump. Bipolar plates with serpentine channels were TA1-type titanium metal plates and guard plates were polyether ether ketone resin. The series resistance of the battery was ca. 0.15 Ω by EIS at open circuit voltages. Steady-state chronopotentiometry was used to plot the polarization curves without *iR* correction. Discharging power density (*P*) was calculated by the following equation.

$$P = E_{cell} \times j \quad (6)$$

Product detection

Determination of ammonia using IC. The concentration of ammonia in the electrolyte was quantified by IC. To be specific, the ammonia standard solution was first used to plot the corresponding standard curve of ionic conductivity as a function of ionic concentrations. Electrolytes after NO_3^-RR electrolysis were immediately diluted by a certain multiple and then directly injected into the IC to measure the ionic conductivity. The corresponding ionic concentration can thus be calculated according to the standard curve. In this work, the cation chromatographic filtrate used by IC was 5 vol% HNO_3. It is noted that considering the produced ammonium by NO_3^-RR electrolysis would cross from catholyte to anolyte through PEM, we thus detected and calculated the sum of ammonia Faradaic efficiencies in both the catholyte and anolyte.

Determination of ammonia using ^1H NMR. The concentration of ammonia in the electrolyte was also quantified by ^1H NMR. $^{14}KNO_3$ and $^{15}KNO_3$ electrolytes were used for NO_3^-RR electrolysis under the same test conditions. After electrolysis, the electrolyte (30 μL) was mixed with hydroquinone (7.5 mM, 10 μL) as an internal standard and deuterated DMSO solvent (400 μL) as solvent for ^1H NMR detection. The quantification of ammonium was determined by comparing the integral area of hydroquinone singlet with that of the $^{14}NH_4^+$ triplet or the $^{15}NH_4^+$ doublet.

Determination of nitrate using IC. The quantification method of nitrate in the electrolyte was almost identical to that of ammonia, except that the anion chromatographic filtrate was replaced by 1 mM $NaHCO_3$ and 3 mM Na_2CO_3 mixed solution, and the suppressor solution of 1 vol% H_3PO_4 was additionally used. It is noted that the electrolyte was alkalized so as to completely ionize nitrous acid before IC measurements.

Determination of hydroxylamine using a UV-Vis spectrophotometer. The concentration of hydroxylamine in the electrolyte was quantified by a UV-Vis spectrophotometer based on the D. S. Frear and R. C. Burrell method[54]. To be specific, the color agent was first prepared by adding certain hydroxylamine hydrochloride standard solution, phosphate-buffered saline solution (0.05 M, 1 mL), trichloroacetic acid solution (12 wt%, 0.2 mL), Na_2CO_3 solution (1 M, 1 mL), and 8-quinolinol ethanol solution (1.25 wt%, 1 mL) in sequence. The color agent was then filled to 5 mL with distilled water and boiled for 1 min. After the color agent cooled down, its absorbance was measured by a UV-Vis spectrophotometer within the wavelength range from 500 to 900 nm, wherein the maximum absorbance was obtained at ca. 708 nm. A series of maximum absorbance was linearly correlated to different hydroxylamine standard concentrations so as to plot the hydroxylamine standard curve. The concentration of hydroxylamine in the electrolyte can thus be quantified by the same protocol according to the plotted hydroxylamine standard curve. It is noted that the pH of the electrolyte was adjusted to neutral before measurements.

Determination of hydrazine using a UV-vis spectrophotometer. The concentration of hydroxylamine in the electrolyte was quantified by a UV-Vis spectrophotometer based on the Watt and Chrisp method[55]. To be specific, 2 g p-dimethylaminobenzaldehyde was first dissolved in 100 mL of ethanol and 10 mL of concentrated hydrochloric acid. Then the color agent was prepared by adding the above solution (4 mL), a certain hydrazine dihydrochloride standard solution, and distilled water to a total of 10 mL. After the color development for 10 min, its absorbance was measured bya UV-Vis spectrophotometer within the wavelength range from 400 to 500 nm, wherein the maximum absorbance was obtained at ca. 460 nm. Then a series of maximum absorbance was linearly correlated to the different hydrazine standard concentrations so as to plot the hydrazine standard curve. The concentration of hydrazine in the electrolyte can thus be quantified by the same protocol according to the plotted hydrazine standard curve.

Determination of hydrogen gas using water drainage. The volume of H_2 was quantified based on the water drainage method. The electrolytic cell was sealed except for one gas outlet, which was connected with an inverted measuring cylinder filled with distilled water. The molar mass of produced H_2 was calculated using the ideal gas state equation.

Theoretical calculation

All the DFT calculations were conducted with the Vienna Ab-initio Simulation Package with the generalized gradient approximation of the Perdew-Burke-Ernzerhof approach[56,57]. 500 eV kinetic energy cutoff and 0.05 eV $Å^{-1}$ Hellmann-force threshold were used for accurate optimization of the structural relaxations. 0.2 eV smearing based on the method of Methfessel-Paxton was used for the total energy calculations. The Brillouin zone integration was performed with 3 × 3 × 1 Monkhorst-Pack *k*-point sampling for geometry relaxation. The atomic coordinates of a Ru/WO_{3-x} heterostructure computational model are displayed in Supplementary Fig. 13. The structure contains 36 W atoms, 107 O atoms, and 32 Ru atoms with a 20 Å vacuum gap along the z-direction. Bader charge analysis was performed to describe the charge variation

quantitatively[58]. Known as a pre- and postprocessing program for the VASP code, VASPKIT was adopted to obtain the DOS diagram[59].

According to the online DEMS result, elemental steps of acidic NO_3^-RR driven by the Ru/WO_{3-x} were simulated as follows:

$$^* + NO_3^- \rightarrow ^* NO_3 + e^- \quad (7)$$

$$^*NO_3 + 2(H^+ + e^-) \rightarrow ^* NO_2 + H_2O \quad (8)$$

$$^*NO_2 + 2(H^+ + e^-) \rightarrow ^* NO + H_2O \quad (9)$$

$$^*NO + H^+ + e^- \rightarrow ^* NHO \quad (10)$$

$$^*NHO + H^+ + e^- \rightarrow ^* NHOH \quad (11)$$

$$^*NHOH + H^+ + e^- \rightarrow ^* NH_2OH \quad (12)$$

$$^*NH_2OH + H^+ + e^- \rightarrow ^* NH_2 + H_2O \quad (13)$$

$$^*NH_2 + H^+ + e^- \rightarrow ^* NH_3 \quad (14)$$

The asterisk (*) represents the reaction active site within the Ru/WO_3. *NO_3, *NO_2, *NO, *NHO, *NHOH, *NH_2OH, *NH_2 and *NH_3 denote the corresponding chemisorbed species upon the NO_3^-RR. Among these eight elementary steps, the first step is the electro-adsorption of NO_3^-, while the rest are the electro-driven hydrogenation steps.

To avoid calculating the energy of charged NO_3^- directly, gaseous HNO_3 is chosen as a reference instead[60]. The adsorption energy of NO_3^- (ΔG_{*NO3}) is described as

$$\Delta G(^*NO_3) = G(^*NO_3) - G(^*) - [G(HNO_3, g) - 1/2G(H_2, g)] + \Delta G_{correct} \quad (15)$$

where $G(^*NO_3)$, $G(^*)$, $G(HNO_3, g)$, and $G(H_2, g)G_{H2(g)}$ are the Gibbs free energy of NO_3^- adsorbed on the substrates, HNO_3, and H_2 molecules in the gas phase, respectively. The free energy correction, $\Delta G_{correct}$, is set to 0.392 eV.

Then, using the computational hydrogen electrode (pH = 0, p = 1 atm, T = 298.15 K), the Gibbs free energy of $H^+ + e^-$ was replaced implicitly with the Gibbs free energy of one-half an H_2 molecule[61].

The electro-adsorption or reaction Gibbs free energy is defined as $\Delta G = \Delta E + \Delta ZPE - T\Delta S$, where ΔE denotes the energy obtained from DFT calculations. ΔZPE and ΔS are the correction of zero-point energy and entropy, respectively. T represents room temperature (298.15 K).

Ab initio molecular dynamics

AIMD simulation was performed via the CP2K program[62]. The PBE functional with the Grimme D3 dispersion correction and the DZVP-MOLOPT-SR basis set with Goedecker-Teter-Hutter pseudo potentials were used[63,64]. The plane wave cutoff energy and relative cutoff were 500 Ry and 50 Ry, respectively. During the AIMD process, canonical sampling through a velocity rescaling thermostat with a time constant of 100 fs was applied in the NVT ensemble. The time step was 0.5 fs. The optimized Ru/WO_{3-x} heterostructure model by VASP was used as the substrate, and the position was fixed, and 50 SO_4^{2-} and 100 H^+ were randomly added to the heterojunction surface by gromacs program as the initial structure of the AIMD simulation[65]. The result was visualized by Visual Molecular Dynamics program[66].

Data availability

Source data are provided with this paper.

References

1. Smith, C., Hill, A. K. & Torrente-Murciano, L. Current and future role of Haber-Bosch ammonia in a carbon-free energy landscape. *Energy Environ. Sci.* **13**, 331–344 (2020).
2. Wang, Y., Wang, C., Li, M., Yu, Y. & Zhang, B. Nitrate electroreduction: Mechanism insight, in situ characterization, performance evaluation, and challenges. *Chem. Soc. Rev.* **50**, 6720–6733 (2021).
3. Xiang, S. et al. New progress of ammonia recovery during ammonia nitrogen removal from various wastewaters. *World J. Microbiol. Biotechnol.* **36**, 144 (2020).
4. Chen, G.-F. et al. Electrochemical reduction of nitrate to ammonia via direct eight-electron transfer using a copper-molecular solid catalyst. *Nat. Energy* **5**, 605–613 (2020).
5. Wu, Q. et al. Screening of transition metal oxides for electrocatalytic nitrate reduction to ammonia at large currents. *Nano Res* **17**, 3902–3910 (2024).
6. Ye, S. et al. Elucidating the activity, mechanism and application of selective electrosynthesis of ammonia from nitrate on cobalt phosphide. *Energy Environ. Sci.* **15**, 760–770 (2022).
7. Dima, G. E., de Vooys, A. C. A. & Koper, M. T. M. Electrocatalytic reduction of nitrate at low concentration on coinage and transition-metal electrodes in acid solutions. *J. Electroanal. Chem.* **554**, 15–23 (2003).
8. Kitano, M. et al. Ammonia synthesis using a stable electride as an electron donor and reversible hydrogen store. *Nat. Chem.* **4**, 934–940 (2012).
9. Khoobiar, S. Particle to particle migration of hydrogen atoms on platinum-alumina catalysts from particle to neighboring particles. *J. Phys. Chem.* **68**, 411–412 (1964).
10. Boudart, M., Vannice, M. A. & Benson, J. E. Adlineation, portholes and spillover. *Z. Phys. Chem.* **64**, 171–177 (1969).
11. Xu, T. et al. Discovery of fast and stable proton storage in bulk hexagonal molybdenum oxide. *Nat. Commun.* **14**, 5490 (2023).
12. Tang, Z. et al. Interfacial hydrogen spillover on Pd-TiO_2 with oxygen vacancies promotes formate electrooxidation. *ACS Energy Lett.* **8**, 3945–3954 (2023).
13. Karim, W. et al. Catalyst support effects on hydrogen spillover. *Nature* **541**, 68–71 (2017).
14. Chen, Z. et al. Hierarchical nanostructured WO_3 with biomimetic proton channels and mixed ionic-electronic conductivity for electrochemical energy storage. *Nano Lett.* **15**, 6802–6808 (2015).
15. Park, J. et al. Investigation of the support effect in atomically dispersed Pt on WO_{3-x} for utilization of Pt in the hydrogen evolution reaction. *Angew. Chem. Int. Ed.* **58**, 16038–16042 (2019).
16. Shao, W. et al. Bioinspired proton pump on ferroelectric HfO_2-coupled Ir catalysts with bidirectional hydrogen spillover for pH-universal and superior hydrogen production. *J. Am. Chem. Soc.* **146**, 27486–27498 (2024).
17. Chen, J. et al. Reversible hydrogen spillover in Ru-WO_{3-x} enhances hydrogen evolution activity in neutral pH water splitting. *Nat. Commun.* **13**, 5382 (2022).
18. Dai, J. et al. Hydrogen spillover in complex oxide multifunctional sites improves acidic hydrogen evolution electrocatalysis. *Nat. Commun.* **13**, 1189 (2022).
19. Jiang, G. et al. Low-loading and highly stable membrane electrode based on an Ir@WO_xNR ordered array for PEM water electrolysis. *ACS Appl. Mater. Interfaces* **13**, 15073–15082 (2021).
20. Jiang, H. et al. Insights on the proton insertion mechanism in the electrode of hexagonal tungsten oxide hydrate. *J. Am. Chem. Soc.* **140**, 11556–11559 (2018).
21. Khyzhun, O. Y., Solonin, Y. M. & Dobrovolsky, V. D. Electronic structure of hexagonal tungsten trioxide: XPS, XES, and XAS studies. *J. Alloy. Compd.* **320**, 1–6 (2001).
22. Khyzhun, O. Y. XPS, XES and XAS studies of the electronic structure of tungsten oxides. *J. Alloy. Compd.* **305**, 1–6 (2000).

23. Shpak, A. P., Korduban, A. M., Medvedskij, M. M. & Kandyba, V. O. XPS studies of active elements surface of gas sensors based on WO_{3-x} nanoparticles. *J. Electron Spectrosc. Relat. Phenom.* **156**, 172–175 (2007).
24. Daniel, M. F., Desbat, B., Lassegues, J. C., Gerand, B. & Figlarz, M. Infrared and raman study of WO_3 tungsten trioxides and WO_3, xH_2O tungsten trioxide tydrates. *J. Solid State Chem.* **67**, 235–247 (1987).
25. Li, P. P., Jin, Z. Y., Fang, Z. W. & Yu, G. H. A single-site iron catalyst with preoccupied active centers that achieves selective ammonia electrosynthesis from nitrate. *Energy Environ. Sci.* **14**, 3522–3531 (2021).
26. Green, C. L. & Kucernak, A. Determination of the platinum and ruthenium surface areas in platinum-ruthenium alloy electrocatalysts by underpotential deposition of copper. I. Unsupported catalysts. *J. Phys. Chem. B* **106**, 1036–1047 (2002).
27. Ji, K. et al. Steering selectivity in electrocatalytic furfural reduction via electrode-electrolyte interface modification. *J. Am. Chem. Soc.* **146**, 11876–11886 (2024).
28. Zheng, X. et al. Tailoring a local acid-like microenvironment for efficient neutral hydrogen evolution. *Nat. Commun.* **14**, 4209 (2023).
29. Cazzanelli, E., Vinegoni, C., Mariotto, G., Kuzmin, A. & Purans, J. Raman study of the phase transitions sequence in pure WO_3 at high temperature and in H_xWO_3 with variable hydrogen content. *Solid State Ion.* **123**, 67–74 (1999).
30. Mitchell, J. B., Lo, W. C., Genc, A., LeBeau, J. & Augustyn, V. Transition from battery to pseudocapacitor behavior via structural water in tungsten oxide. *Chem. Mater.* **29**, 3928–3937 (2017).
31. Wei, C. et al. Recommended practices and benchmark activity for hydrogen and oxygen electrocatalysis in water splitting and fuel cells. *Adv. Mater.* **31**, 1806296 (2019).
32. Feng, C. et al. Triple synergy engineering via metal-free dual-atom incorporation for self-sustaining acidic ammonia electrosynthesis. *Angew. Chem. Int. Ed.* **64**, e202505211 (2025).
33. Ba, J. et al. Red carbon mediated formation of Cu_2O clusters dispersed on the oxocarbon framework by Fehling's route and their use for the nitrate electroreduction in acidic conditions. *Adv. Mater.* **36**, 2400396 (2024).
34. Cheng, Q. et al. Multivariate covalent organic frameworks with tailored electrostatic potential promote nitrate electroreduction to ammonia in acid. *Nat. Commun.* **16**, 3717 (2025).
35. Chen, H. et al. Conductive polymer protection strategy to promote electrochemical nitrate reduction to ammonia in highly acidic condition over Cu-based catalyst. *Chem. Eng. J.* **481**, 148596 (2024).
36. Zhang, R. et al. Electrochemical nitrate reduction in acid enables high-efficiency ammonia synthesis and high-voltage pollutes-based fuel cells. *Nat. Commun.* **14**, 8036 (2023).
37. Lv, Y. et al. Highly efficient electrochemical nitrate reduction to ammonia in strong acid conditions with Fe_2M-trinuclear-cluster metal-organic frameworks. *Angew. Chem. Int. Ed.* **62**, e202305246 (2023).
38. Jia, R. R. et al. Boosting selective nitrate electroreduction to ammonium by constructing oxygen vacancies in TiO_2. *ACS Catal.* **10**, 3533–3540 (2020).
39. Xiao, Z. et al. Bifunctional Co_3S_4 nanowires for robust sulfion oxidation and hydrogen generation with low power consumption. *Adv. Funct. Mater.* **33**, 2212183 (2022).
40. Yu, W. et al. Laser-controlled tandem catalytic sites of CuNi alloys with ampere-level electrocatalytic nitrate-to-ammonia reduction activities for Zn-nitrate batteries. *Energy Environ. Sci.* **16**, 2991–3001 (2023).
41. Zhu, W. et al. Weakened d-p orbital hybridization in in situ reconstructed Ru/β-$Co(OH)_2$ heterointerfaces for accelerated ammonia electrosynthesis from nitrates. *Energy Environ. Sci.* **16**, 2483–2493 (2023).
42. Lin, W., Zhou, E., Xie, J. F., Lin, J. & Wang, Y. A high power density Zn-nitrate electrochemical cell based on theoretically screened catalysts. *Adv. Funct. Mater.* **32**, 2209464 (2022).
43. Jiang, H. et al. Enabled efficient ammonia synthesis and energy supply in a zinc-nitrate battery system by separating nitrate reduction process into two stages. *Angew. Chem. Int. Ed.* **62**, e202218717 (2023).
44. Nangan, S., Ding, Y., Alhakemy, A. Z., Liu, Y. & Wen, Z. Hybrid alkali-acid urea-nitrate fuel cell for degrading nitrogen-rich wastewater. *Appl. Catal. B: Environ.* **286**, 121291 (2021).
45. Zhu, W. et al. A hydrazine-nitrate flow battery catalyzed by a bimetallic RuCo precatalyst for wastewater purification along with simultaneous generation of ammonia and electricity. *Angew. Chem. Int. Ed.* **62**, e202300390 (2023).
46. Wang, D. et al. Hexagonal cobalt nanosheets for high-performance electrocatalytic NO reduction to NH_3. *J. Am. Chem. Soc.* **145**, 6899–6904 (2023).
47. Liang, J. et al. Amorphous boron carbide on titanium dioxide nanobelt arrays for high-efficiency electrocatalytic NO reduction to NH_3. *Angew. Chem. Int. Ed.* **61**, e202202087 (2022).
48. Zhang, L. et al. High-performance electrochemical NO reduction into NH_3 by MoS_2 nanosheet. *Angew. Chem. Int. Ed.* **60**, 25263–25268 (2021).
49. Qi, D. et al. High-efficiency electrocatalytic NO reduction to NH_3 by nanoporous VN. *Nano Res. Energy* **1**, 9120022 (2022).
50. An, S. et al. Multi-functional formaldehyde-nitrate batteries for wastewater refining, electricity generation, and production of ammonia and formate. *Angew. Chem. Int. Ed.* **63**, e202318989 (2024).
51. Pei, Y. et al. High-entropy sulfide catalyst boosts energy-saving electrochemical sulfion upgrading to thiosulfate coupled with hydrogen production. *Angew. Chem. Int. Ed.* **136**, e202411977 (2024).
52. Liang, H. et al. Tungsten blue oxide as a reusable electrocatalyst for acidic water oxidation by plasma-induced vacancy engineering. *CCS Chem.* **3**, 1553–1561 (2021).
53. Gao, L. N. et al. High-performance energy-storage devices based on WO_3 nanowire arrays/carbon cloth integrated electrodes. *J. Mater. Chem. A* **1**, 7167–7173 (2013).
54. Frear, D. S. & Burrell, R. C. Spectrophotometric method for determining hydroxylamine reductase activity in higher plants. *Anal. Chem.* **27**, 1664–1665 (1955).
55. Watt, G. W. & Chrisp, J. D. Spectrophotometric method for determination of hydrazine. *Anal. Chem.* **24**, 2006–2008 (1952).
56. Perdew, J. P. et al. Restoring the density-gradient expansion for exchange in solids and surfaces. *Phys. Rev. Lett.* **100**, 136406 (2008).
57. Perdew, J. P., Burke, K. & Ernzerhof, M. Generalized gradient approximation made simple. *Phys. Rev. Lett.* **77**, 3865–3868 (1996).
58. Tang, W., Sanville, E. & Henkelman, G. A grid-based bader analysis algorithm without lattice bias. *J. Phys. Condens. Matter* **21**, 084204 (2009).
59. Wang, V., Xu, N., Liu, J.-C., Tang, G. & Geng, W.-T. Vaspkit: A user-friendly interface facilitating high-throughput computing and analysis using vasp code. *Comput. Phys. Commun.* **267**, 108033 (2021).
60. Liu, J.-X., Richards, D., Singh, N. & Goldsmith, B. R. Activity and selectivity trends in electrocatalytic nitrate reduction on transition metals. *ACS Catal.* **9**, 7052–7064 (2019).
61. Nørskov, J. K. et al. Origin of the overpotential for oxygen reduction at a fuel-cell cathode. *J. Phys. Chem. B* **108**, 17886–17892 (2004).
62. Hutter, J., Iannuzzi, M., Schiffmann, F. & VandeVondele, J. Cp2k: Atomistic simulations of condensed matter systems. *Wiley Interdiscip. Rev.: Comput. Mol. Sci.* **4**, 15–25 (2014).

63. VandeVondele, J. & Hutter, J. Gaussian basis sets for accurate calculations on molecular systems in gas and condensed phases. *J. Chem. Phys.* **127**, 114105 (2007).
64. Hartwigsen, C., Goedecker, S. & Hutter, J. Relativistic separable dual-space Gaussian pseudopotentials from H to Rn. *Phys. Rev. B* **58**, 3641–3662 (1998).
65. Berendsen, H. J. C., van der Spoel, D. & van Drunen, R. Gromacs: A message-passing parallel molecular dynamics implementation. *Comput. Phys. Commun.* **91**, 43–56 (1995).
66. Humphrey, W., Dalke, A. & Schulten, K. VMD: Visual molecular dynamics. *J. Mol. Graph.* **14**, 33–38 (1996).

Acknowledgements

This work was funded by National Key Research and Development Program of China (Grant No.: 2023YFB4004700, H. L.), Natural Science Foundation of Xiamen, China (Grant No.: 3502Z202473021, H. L.), Fundamental Research Funds for the Central Universities of China (Grant No.: 20720240066, H. L.), Basic Research Program of Jiangsu (Grant No.: BK20251079, W. Z.), Natural Science Research Project of Higher Education Institutions in Jiangsu Province (Grant No.: 25KJB150032, W. Z.), National Science and Technology Council in Taiwan (Grant No.: NSTC 114-2112-M-213-026-MY3; 114-2221-E-213-001-MY3, Y-G. L.), National Synchrotron Radiation Research Center in Taiwan(Y-G. L.), National Natural Science Foundation of China (Grant No.: 52501281, F. Y.), Natural Science Foundation of Jilin Province (Grant No.: YDZJ202301ZYTS296, F. Y.) and the Research Program on Science and Technology from the Education Department of Jilin Province (Grant No.: JJKH20240558KJ, F. Y.).

Author contributions

W. Z. and H. L. conceived the project and wrote the paper. W. Z. and J. L. conducted the physical characterizations and electrochemical tests. Y-C. L. and Y.-G. L. conducted and analyzed the XAS experiments. M. Z. synthesized the catalysts. J. C., C. H., J. J. and F. Y. conducted and analyzed the AIMD and DFT calculations. X. W., Y. H., and G. Y. helped the material characterization and analysis. All authors contributed to the general discussion. W. Z., Y.-C. L., J. C., and M. Z. contributed equally to this work.

Competing interests

The authors declare no competing interests.

Additional information

Supplementary information The online version contains supplementary material available at https://doi.org/10.1038/s41467-026-69335-x.

Correspondence and requests for materials should be addressed to Yan-Gu Lin, Gang Yang, Fen Yao or Hanfeng Liang.

Peer review information *Nature Communications* thanks Wenhui He and the other anonymous reviewer(s) for their contribution to the peer review of this work. A peer review file is available.